2009

Investigations of an innovative combined cycle nozzle

Dustin E. Wood

INVESTIGATIONS OF AN INNOVATIVE COMBINED CYCLE NOZZLE

by

DUSTIN E. WOOD

A THESIS

Submitted in partial fulfillment of the requirements
for the degree of Master of Science in Engineering
in
The Department of Mechanical & Aerospace Engineering
to
The School of Graduate Studies
of
The University of Alabama in Huntsville

HUNTSVILLE, ALABAMA

2009

In presenting this thesis in partial fulfillment of the requirements for a master's degree from The University of Alabama in Huntsville, I agree that the Library of this University shall make it freely available for inspection. I further agree that permission for extensive copying for scholarly purposes may be granted by my advisor or, in his/her absence, by the Chair of the Department or the Dean of the School of Graduate Studies. It is also understood that due recognition shall be given to me and to The University of Alabama in Huntsville in any scholarly use which may be made of any material in this thesis.

Dustin Wood

Dustin E. Wood

6/30/09

Date

THESIS APPROVAL FORM

Submitted by Dustin E. Wood in partial fulfillment of the requirements for the degree of Master of Science in Engineering in Aerospace Engineering and accepted on behalf of the Faculty of the School of Graduate Studies by the thesis committee.

We, the undersigned members of the Graduate Faculty of The University of Alabama in Huntsville, certify that we have advised and/or supervised the candidate on the work described in this thesis. We further certify that we have reviewed the thesis manuscript and approve it in partial fulfillment of the requirements of the degree of Master of Science in Engineering in Aerospace Engineering.

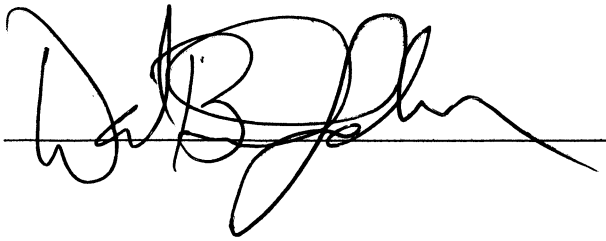

6/22/09 (Date) Committee Chair

Robert A. Dziedzic 06/22/09 (Date) Member

06/22/09 (Date) Member

6/27/09 (Date) Department Chair

6/30/10 (Date) College Dean

Debra M. Mauriello 7/28/09 (Date) Graduate Dean

ABSTRACT

The School of Graduate Studies

The University of Alabama in Huntsville

Degree Master of Science in Engineering College/Dept. Engineering/Mechanical and. Aerospace Engineering .

Name of Candidate Dustin Eugene Wood .

Title Investigations of an Innovative Combined Cycle Nozzle .

The Rocket Plug Nozzle Combined Cycle (RPNCC) Propulsion System was conceived to alleviate some of the inherent disadvantages of conventional Rocket Based Combined Cycle systems. A rapid, relatively accurate method was needed to model the coaxial jets of the RPNCC system. This thesis describes modification and integration of an empirical base pressure correlation into the Aerospike Design and Performance Tool (ADAPT) to estimate performance of the RPNCC system. Accounting for geometric and flow field effects improved the base pressure prediction to within 10% of existing experimental data. The modified ADAPT code was used in a first-order system comparison of a missile using the RPNCC system to the performance of conventional airbreathing and solid rocket propulsion systems. In this application, the RPNCC system was heavier and reduced overall mission performance. However, this novel concept may be of benefit when replacing conventional liquid rocket or RBCC systems in a space launch vehicle application.

Abstract Approval: Committee Chair 6/22/09

Department Chair 6/27/09

Graduate Dean 7/28/09

ACKNOWLEDGMENTS

The work described in this thesis would not have been possible without the assistance of a number of people. First, I would like to thank my advisor, Dr. Brian Landrum, for his patience and guidance during my pursuit of this degree. I would like to thank Dr. Jim Blackmon and Dr. Michael Benfield for guidance in the preliminary propulsion systems study, and Olivier Demaneuf for running preliminary computational fluid dynamic cases. I would also like to thank Mr. Sheldon Smith for providing advice on the use and modification of the Aerospike Design and Performance Tool source code. Finally, I would like to thank the Alabama Space Grant Consortium for providing me with the funding to pursue this degree.

TABLE OF CONTENTS

LIST OF FIGURES

LIST OF TABLES

LIST OF ABBREVIATIONS / ACRONYMS

1-D	One-dimensional
2-D	Two-dimensional
3-D	Three-dimensional
ADAPT	Aerospike Design and Performance Tool
ATACMS	Army Tactical Missile System
BLIMPJ	Boundary Layer Integral Matrix Procedure J
CAV	Common Aerial Vehicle
CCP	Combined Cycle Propulsion
CEC	Chemical Equilibrium Code
CFD	Computational Fluid Dynamics
DARPA	Defense Advanced Research Program Agency
DOF	Degree of Freedom
IRR	Integrated Rocket Ramjet
Isp	Specific Impulse
MOC	Method of Characteristics
MSFC	Marshall Space Flight Center
NASA	National Aeronautics and Space Administration
NPR	Nozzle Pressure Ratio
RBCC	Rocket Based Combined Cycle
RMF	Momentum Flux Ratio
RPNCC	Rocket Plug Nozzle Combined Cycle

SFC	Specific Fuel Consumption
UAH	The University of Alabama in Huntsville

LIST OF SYMBOLS

A	Area
a	Speed of Sound
C_T	Thrust Coefficient
d	Diameter
M	Mach Number
P	Pressure
q	Dynamic Pressure
R	Radial Coordinate
T	Temperature
V	Velocity
X	Axial Coordinate
β	Shock Wave Angle
γ	Ratio of Specific Heat
ρ	Density
$\dot{m}$	Mass Flow Rate
θ	Flow Turning Angle
ν	Prandtl-Meyer Function

SUBSCRIPTS

∞	Freestream
a	Parameters After the Expansion/Shock System
B	Base Parameters
oj	Total Jet Parameters
j	Jet Exit Parameters
ref	Reference Parameters

CHAPTER 1

INTRODUCTION

1.1 Advanced Launch Vehicle Propulsion Systems

There is a need for innovative techniques to increase the efficiencies and capabilities of launch vehicle propulsion systems, above current technology. Historically staging space launch vehicles, like the Saturn V rocket [1], has been proven to increase the system's payload to orbit and overall effective specific impulse (*Isp*) [2]. This is primarily due to disposing the inert mass of the burnt out stage so that the remaining flight vehicle can continue to accelerate without the excess weight. Determining the number of stages is typically a trade off between decreasing the inert mass of the vehicle and increasing cost and complexity [3].

As an alternative to staging, launch vehicle designers proposed a conventional horizontal takeoff to orbital insertion by simply adding rocket engine or airbreathing "pods" to the wings or fuselage. However, this approach significantly increased the cross-sectional area of the flight vehicle, thus increasing the aerodynamic drag, especially in the transonic flight regime. To solve this problem it was proposed to combine the rocket and airbreather engines into a single flow path. Incorporating airbreathing engines also made it possible to reduce the size of the required oxidizer tanks for the overall

propulsion system. Integrating several different propulsion modes within the same flow path is often referred to as a combined cycle or composite engine [4].

The basic principle of combined cycle propulsion (CCP) is to operate the engine in the propulsion mode that provides the highest *Isp* or lowest specific fuel consumption (SFC) for each particular flight condition [5]. For example, a vehicle powered by an airbreathing-rocket combination could use the air-augmented rocket mode for take-off and accelerate to around Mach 2, transition to more efficient ramjet or scramjet airbreathing modes for supersonic to hypersonic cruise, and then transition to a pure rocket mode for final acceleration into orbit. An engine with all the capabilities necessary to fly a vehicle into orbit in a single stage is well beyond current technology. However, a CCP system implemented in a missile configuration could provide more efficient initial boost, rocket thrust augmentation of the airbreather, a high-speed dash, or help to increase kinetic energy at impact with a target.

1.2 Current Applications of Combined Cycle Propulsion

Typically, the technology used for long-range missiles or aircraft is later adapted to launch vehicle applications after the cheaper development of an unmanned system has proven the technology reliable. This evolution can be seen within technology development programs like the X-51 hypersonic wave rider program with the U.S. Air Force [6]. In this system a solid propellant Army Tactical Missile System (ATACMS) booster will be attached in a tandem configuration to accelerate the flight vehicle up to velocities at which the scramjet can operate for sustained powered flight. At burn out the booster will separate and fall back to earth, while the X-51 flight vehicle continues under

its own airbreathing power at hypersonic speeds. For military design projects, cost is usually the ultimate discriminating factor among designs. However, a crucial element in determining a final flight vehicle design is based on assessing its performance and operating characteristics with different propulsion systems, such as a tandem booster or integrated rockets [7].

Generic types of combined cycle configurations are already in use in military applications, such as surface-to-air, surface-to-surface, and supersonic cruise missiles. Figure 1.1 shows a traditional canister type liquid or gaseous fueled ramjet with a tandem solid propellant booster. This configuration is analogous to the X-51 configuration. The tandem booster provides the initial thrust to achieve ramjet initiation speed, typically around Mach 1.5 or 2. For the traditional ramjet, the incoming supersonic air is diffused to a subsonic speed through a shock train before reaching the combustion chamber, at which point, fuel is injected and burned with the air and reaccelerated through the exit nozzle to produce thrust. Most subsonic combustion ramjets operate in the Mach 1.5 to 5 speed range, whereas the supersonic combustion ramjet or scramjet engine can operate at speeds above Mach 5 and can theoretically reach orbital speeds [7, 8, 9].

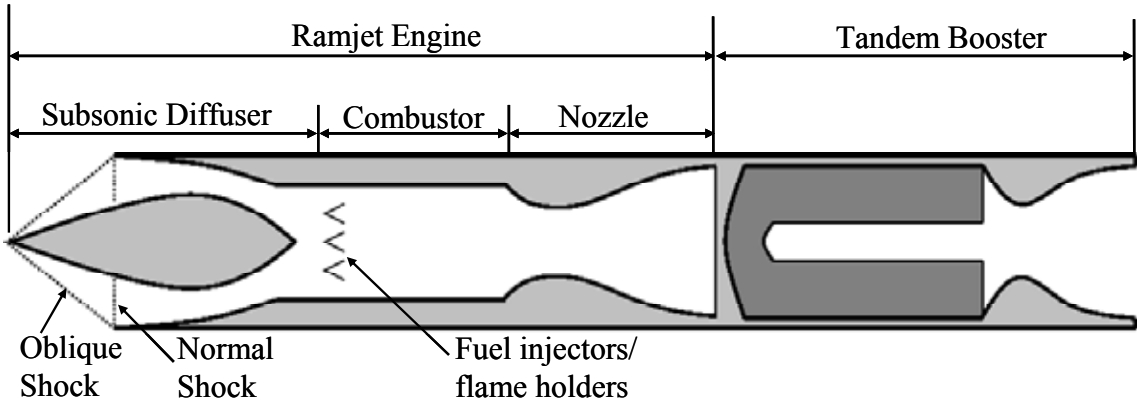

Figure 1.1: Tandem Solid Booster with Canister Ramjet Configuration.

An alternative to the traditional canister ramjet with tandem booster is the integrated rocket ramjet (IRR), in which both the booster and ramjet share a common combustion chamber. Figures 1.2 and 1.3 depict solid and liquid fuel IRR configurations, respectively. Solid-fueled ramjets offer simplicity of the fuel supply and storage. However, if the ability to throttle the engine thrust is desired in the airbreather or rocket cycle, a liquid-fueled system is required.

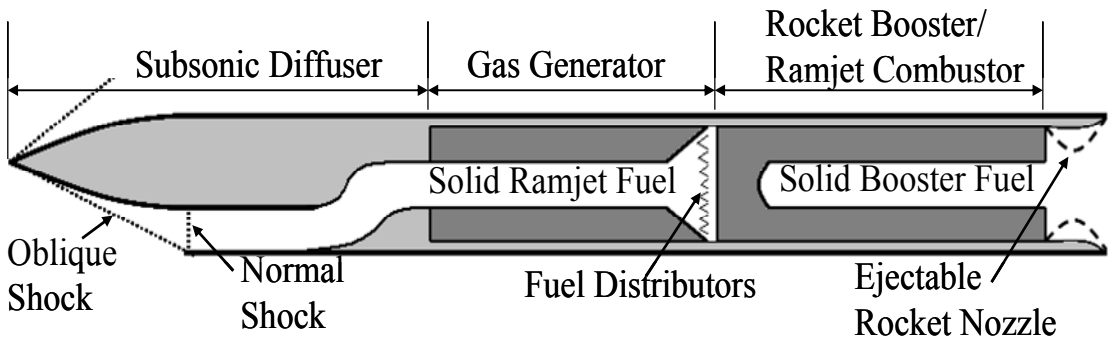

Figure 1.2: Solid Fuel Integral-Rocket Ramjet (IRR) Configuration.

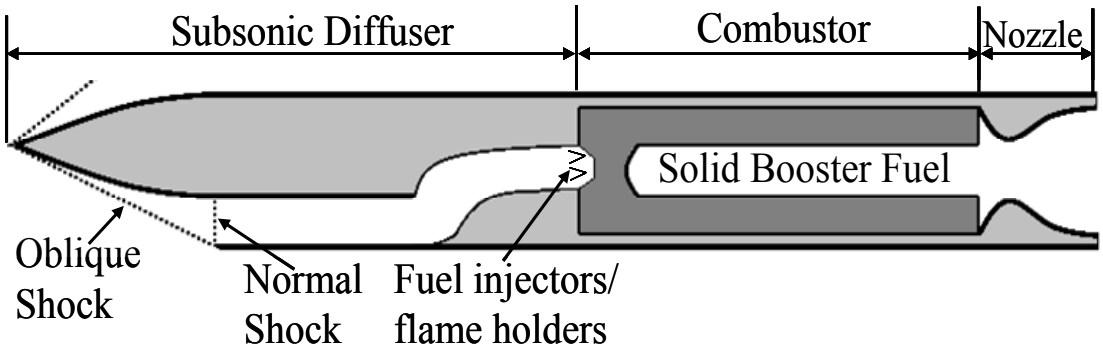

Figure 1.3: Liquid Fuel Integral-Rocket Ramjet (IRR) Configuration.

A compromise between the simplicity of the solid-fuel IRR and the throttle-ability of the liquid-fueled ramjet is the air-ducted rocket shown in Figure 1.4. This particular propulsion system uses a fuel-rich monopropellant to generate a moderately low-pressure gaseous fuel supply for the subsonic combustor and is generally used when the SFC does not adversely affect the powered range [9]. Of all the propulsion systems presented here, the liquid-fueled ramjet system always exhibits superior performance over the other concepts [8, 9].

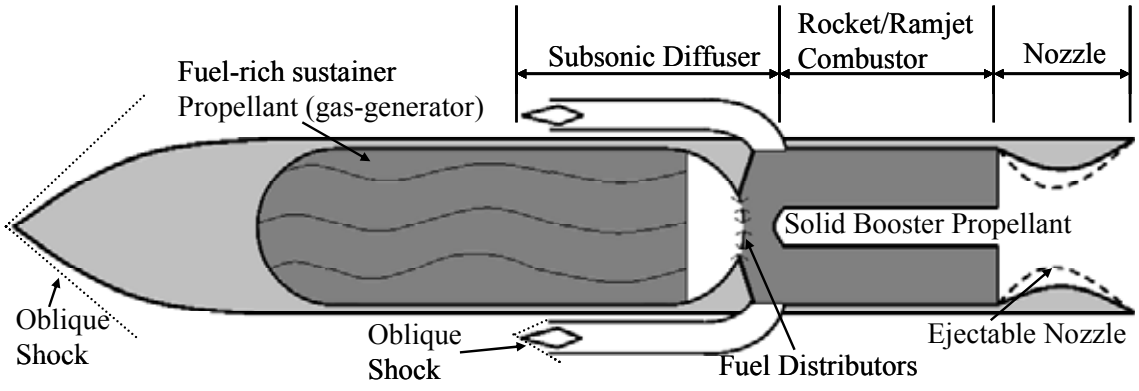

Figure 1.4: Air-Ducted Rocket Configuration.

Ramjet engine cycles for the configurations shown in Figures 1.1 to 1.4 cannot produce net positive static thrust, which is why they all require a booster to accelerate the airbreather up to operating speed. When launching a flight vehicle over land, safety concerns also require that a separated stage or an ejected nozzle not fall back to earth over populated areas. This is partially why most surface launched missiles are fired on or near a coast line or off a military ship, so that the booster stage poses no threat to personnel.

To overcome deficiencies of the configurations discussed to this point and still maintain high mission performance, other general combined cycle ramjet engine concepts have been proposed. The first concept is an air-turbo ramjet (Figure 1.5) wherein a rotating air compressor is added ahead of the combustor and a turbine to drive the compressor is placed downstream of the combustor [7]. An afterburner can be used to increase thrust and acceleration from static conditions. But, this typically increases the fuel consumption significantly. The turbojet mode is similar to a booster stage in that once the flight vehicle reaches a high enough Mach number, the ramjet takes over as the main propulsion mode. The main difference from the tandem booster is that the turbojet is not ejected after the ramjet takes over. But, the added weight of the rotating turbojet machinery must be balanced by a reduced fuel requirement to compete with the simpler solid rocket booster [7, 8, 9]. Billig [7] has shown that for Mach numbers below three, the Carnot efficiency of the turbojet cycle is higher due to the pressure rise of the compressor and fuel is saved relative to the solid booster. However, the use of a turbojet is dependent on the type of mission the flight vehicle is to perform. Due to a turbojet's

increased complexity, it usually leads to higher system costs when compared to a much simpler tandem or integral solid booster [7, 8, 9].

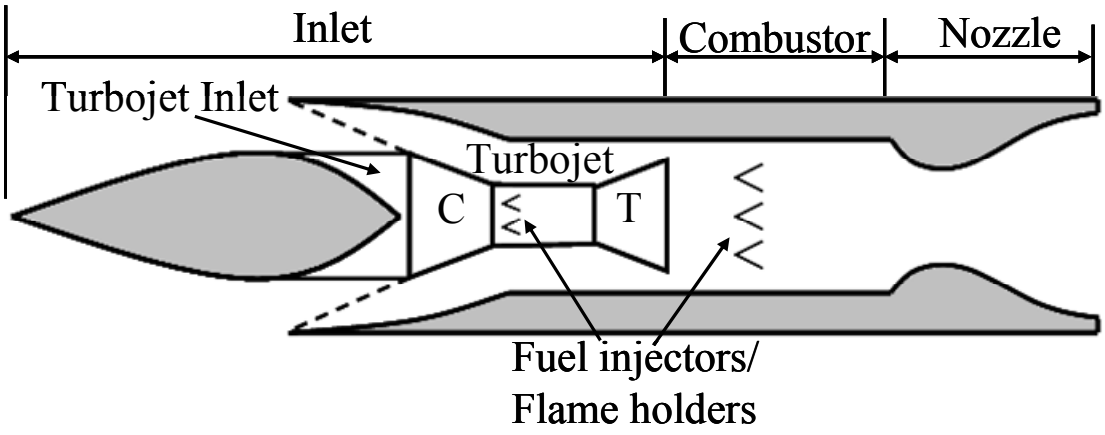

Figure 1.5: Turbo-Ramjet Configuration.

A second combined cycle concept is the ejector ramjet or conventional rocket based combined cycle propulsion system (Figure 1.6). This variant consists of an internal rocket motor that produces high-pressure, fuel-rich, supersonic flow that creates an ejector effect and draws in secondary air into the engine, even at static conditions [7, 8, 9]. The fuel-rich rocket exhaust and ingested air mixture burns at subsonic speeds through the remainder of the duct before being expanded through the convergent-divergent exit nozzle. This produces the net positive thrust required for acceleration from static conditions. In this way, the internal rocket produces enough thrust for initial acceleration of the flight vehicle to a velocity at which air can enter the inlet with enough mass flow and pressure to mix with the fuel rich rocket exhaust, burn in the combustor, and accelerate through the nozzle to provide sustained thrust. There are several other

variants of the turbojet, ramjet, and scramjet that are not included here for the sake of brevity and because they are specialized subsets of the above propulsion cycles [7, 8, 9].

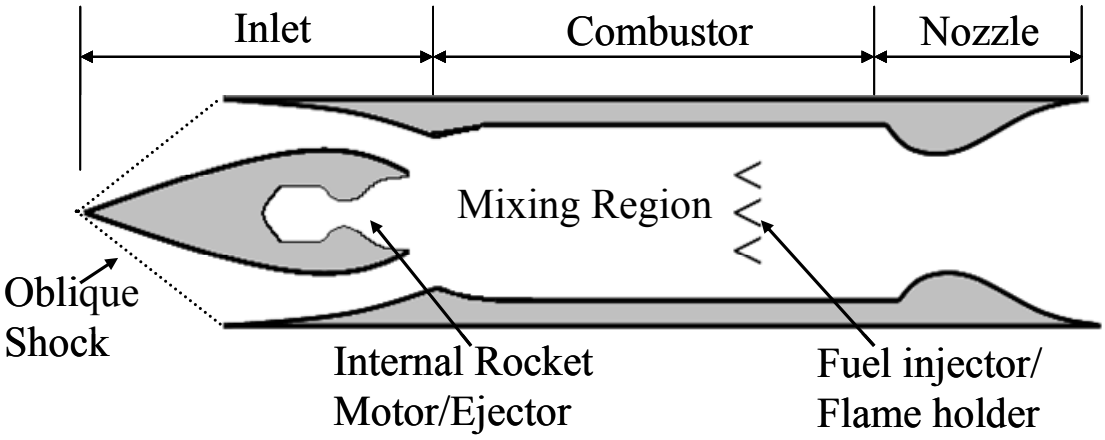

Figure 1.6: Ejector Ramjet or Rocket Based Combined Cycle Configuration.

1.3 Rocket Plug Nozzle Combined Cycle Propulsion System

While conventional CCP systems may provide performance improvements for launch vehicles, incorporating the various engine modes into one flow path creates a number of operational and packaging challenges. As the engine transitions between modes, the inlet geometry must adapt to produce a change in flow path area to ingest the proper mass flow of air and ensure maximum shock capture at a wide range of Mach numbers. The internal geometry must also change shape and dimensions for proper internal flow control [10]. For combined cycle engines with an internal rocket, this geometry change may be even more complex for the ram/scramjet modes. The geometric changes require large, complex drive mechanisms with an associated weight penalty.

Different sets of injection and flame holding devices are required along the mixing duct for the initial air-augmented rocket, ramjet, and scramjet operation.

These mechanisms and control requirements impose operational penalties on the rocket-based CCP system, introduce drag throughout the entire flight profile, and decrease the overall efficiency of the system. This makes a system with a rocket motor internal to the airbreather a challenge both technologically and operationally. For manned or scientific missions, it is also desirable for the engine mode transitions to be relatively smooth and avoid sharp changes in thrust or acceleration. Finally, the number of engines and the optimum positioning of the internal rocket engine components and propellant tanks complicate the design process even further.

The Rocket Plug Nozzle Combined Cycle (RPNCC) Propulsion System [11] was conceived to help alleviate some if not all of the inherent disadvantages of the conventional RBCC configurations. The RPNCC configuration (Figure 1.7) consists of an external annular plug nozzle rocket engine surrounding an airbreathing engine (a ramjet, scramjet, or a turbo-ramjet) placed within the central plug body. The airbreathing engine exhausts through the plug base such that the interaction between it and the rocket engines occurs only at the exhaust. Unlike the conventional RBCC configuration shown in Figure 1.6, there are no additional internal flow field complexities in the operation of the two engines throughout the flight regime. The RPNCC system can potentially achieve more efficient packaging and reduced drag, while also providing rocket nozzle altitude compensation. The RPNCC configuration also could provide smooth engine operating mode transitions and improvements in overall engine performance.

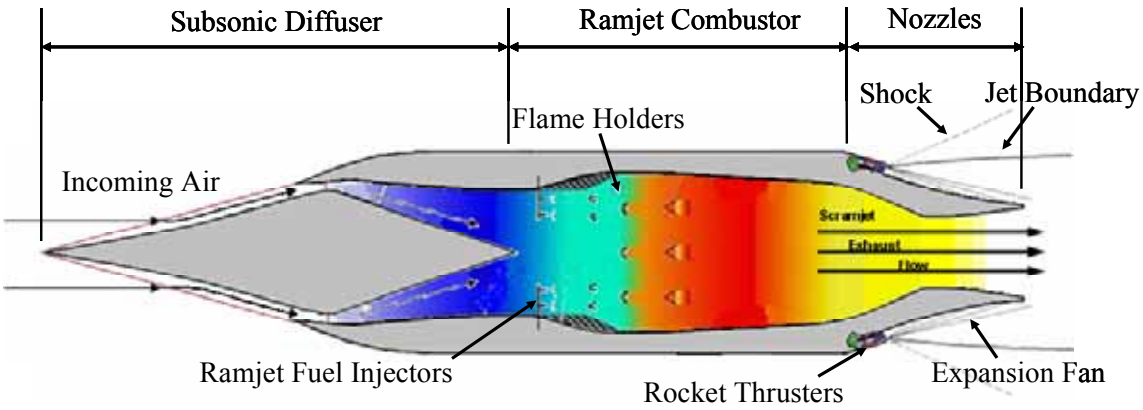

Figure 1.7: The RPNCC Concept Flowpath.

1.4 Research Objectives

To investigate the RPNCC concept, it was desired to rapidly assess and optimize the system's performance and mission impact and compare these results with other CCP systems. To do this, tools that could evaluate the unique nozzle configuration were needed. It was determined that the available computational methods were too time restrictive and would not be easily integrated into design optimizations. However, an analytical tool did exist for rapidly assessing plug nozzle geometry and performance called the Aerospike Design and Performance Tool (ADAPT) [12]. By modifying ADAPT to model the co-axial flows of the RPNCC nozzle configuration and to account for base pressure losses, it could be used to quickly determine performance parameters of the RPNCC system with reasonable accuracy. It could also be combined with other multi-disciplinary design optimization tools to quantify the benefits of this unique CCP system concept in various mission scenarios.

The primary focus of this thesis is the modification and integration of an empirical base pressure correlation into ADAPT to rapidly evaluate the impact of the

RPNCC propulsion system on flight vehicle mission performance. The use of the modified ADAPT code is then demonstrated in a first order systems level analyses of an RPNCC powered missile.

CHAPTER 2

ROCKET PLUG NOZZLE COMBINED CYCLE CONFIGURATION

2.1 Plug Nozzle Characterization

The first and most obvious advantage of the RPNCC concept is the use of a truncated isentropic plug or aerospike rocket nozzle. Despite the proven legacy of the conventional bell rocket nozzle shape (Figure 2.1), it can only be designed for optimum performance at one altitude because of the fixed contour and design exit area. A bell nozzle designed for higher altitudes will not perform as well at low altitudes and vice-versa [2]. At the design altitude, exhaust gases exit the nozzle in a column like shape similar to line IE in Figure 2.1. Below the design altitude, where the ambient pressure is higher than the nozzle exit pressure, a bell nozzle is over-expanded and the plume is usually characterized by line OE in Figure 2.1. Over-expansion can cause separation and normal shocks or Mach disks to appear inside the nozzle. Above the design altitude, where the ambient pressure is lower than the nozzle exit pressure, a bell nozzle is under-expanded. This causes the plume to expand beyond the nozzle skirt as shown by line UE in Figure 2.1. Bell nozzles that have the ability to compensate for changes in atmospheric pressure associated with altitude changes are very complex, requiring variable nozzle exhaust skirts. These additional features increase cost and weight, further

complicate integration into flight vehicles, can lead to reduced reliability and life, and can increase the uncertainty in the overall design of the propulsion system.

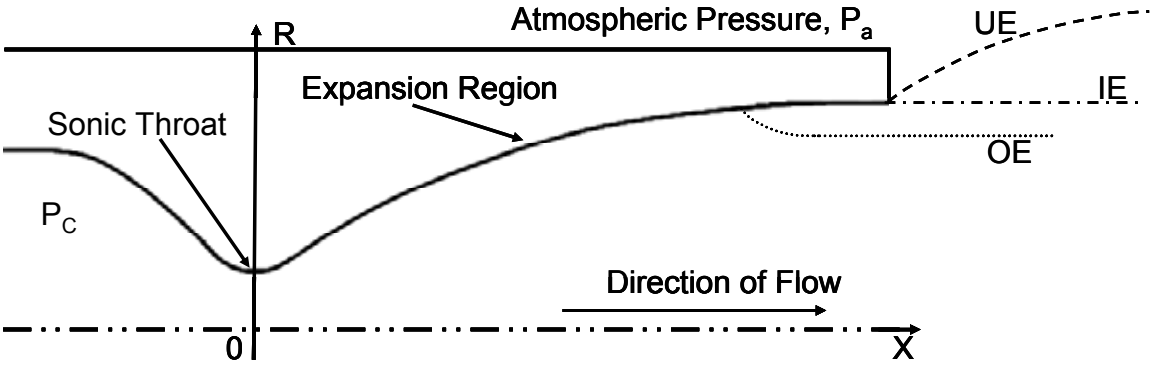

Figure 2.1: Bell Shaped Nozzle and Plume Characterization.

The isentropic plug or aerospike nozzle is an external expansion nozzle, first proposed by the Rocketdyne Corporation, which expands the rocket plume in an approximately isentropic fashion to the atmospheric pressure at that altitude [13]. This allows the nozzle expansion to compensate for pressure changes associated with the increasing altitude of the rocket ascent. The altitude compensation capability of the plug nozzle also reduces thrust losses and maintains a nearly optimum performance at any altitude.

A drawback to the "ideal" plug nozzle is that the fully isentropic expansion requires an excessively long and heavy spike. However, since the nozzle pressure components near the end of the spike contribute very little to the axial thrust, this portion of the spike can be truncated to help reduce weight. Figure 2.2 shows the geometry and terms associated with an isentropic plug nozzle. The "ideal" spike contour terminates at

a vertex, point X on the central axial line. Truncating the contour forms a base region, noted by the line DC. The throat of a plug nozzle is located at the cowl lip, where the expansion process begins down the contour of the plug.

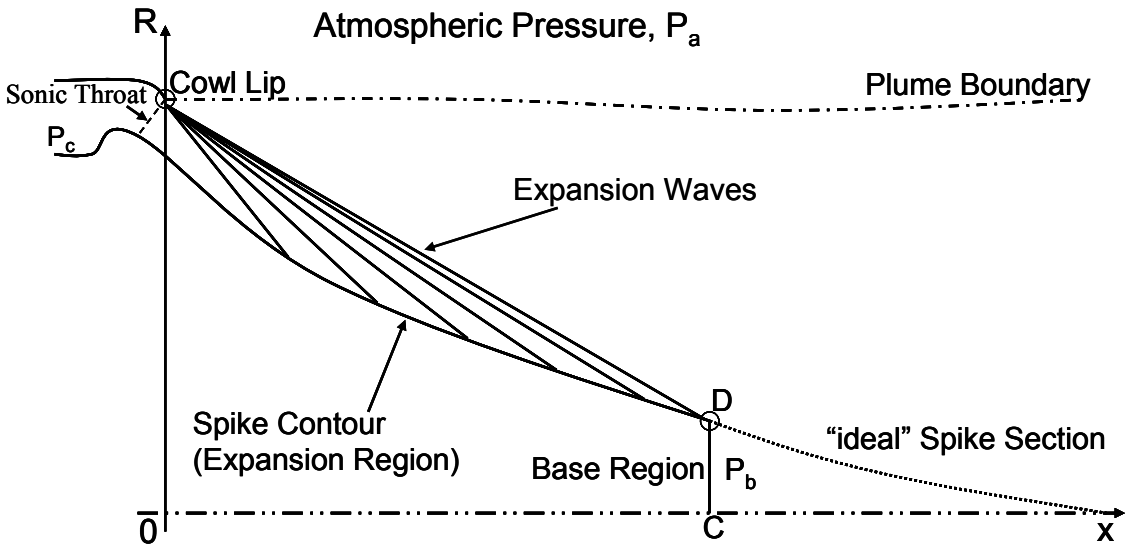

Figure 2.2: Plug Nozzle Nomenclature and Physical Features at Design Altitude.

During the 1950's Dr. G.R. Rao derived a way to calculate the contour of a bell nozzle to give maximum thrust for a specified length, which became known as the minimum length nozzle [14]. He later applied this method to determining a plug nozzle contour for a specified length and altitude [13]. The Method of Characteristics (MOC) [15] is used to construct the plug nozzle contour to allow for the exhaust gases to expand isentropically to the exit of the ramp, located in Figure 2.2 by point D. Therefore, the radius of the cowl lip and contour of the ramp are varied to meet the given requirements of length, throat area, and design altitude or ambient atmospheric pressure. Also, because

the length is a prescribed parameter, the contour does not terminate at a vertex on the center axis, but instead ends at the nozzle base region.

The analytical computer code described in the next chapter uses the MOC to specify supersonic nozzles and predict the flow field properties and performance of the nozzles. The MOC is a marching-type numerical method for determining flow field properties in a continuous supersonic flow [16]. The concept can be described as following a physical disturbance in a supersonic flow field, as it propagates along the Mach lines or characteristics in the flow. The governing partial differential equations along the characteristic, the continuity, momentum, and energy equations, reduce to total differential equations, known as the compatibility equations, which the dependent variable must satisfy. These equations can be solved in a step-by-step method, called the unit process, along the characteristic to solve for the corresponding properties in a down stream manner. For more detail on the derivation of the compatibility equations and the unit process, the reader is referred to Anderson [15], and Zucrow and Hoffman [16], both of whom have written extensively on using MOC for two-dimensional and axisymmetric, irrotational flows for constructing supersonic nozzle geometries.

The base region on an aerospike is typically dominated by subsonic recirculating flow caused by the primary exhaust flowing over the backward facing step. This recirculating flow lowers the base pressure (increasing drag), increases heat transfer from the rocket exhaust to the base region, and reduces the potential performance increases of allowing the flow to expand isentropically over the ramp. However, the base pressure can be increased by injecting low momentum gas through the base in a process known as ‘base-bleed’. By providing a way to pressurize the base region, the loss of performance

from truncating the spike can be nullified. This also helps in alleviating some of the heat transferred from the exhaust gases [17].

A truncated plug contour or aerospike is also designed for a particular altitude. The base region can be defined as having an open or closed wake based on being above or below the design altitude of the contour. Just above the design altitude, the first expansion wave from the cowl lip moves off the end of the spike contour and closes the wake behind the base region. In a closed wake, the base pressure is independent of the atmospheric pressure and depends only on the exit pressure of the aerospike flow. Below the design altitude, all the expansion waves emanating from the cowl lip strike the spike contour, leaving the wake open and causing the base region and its associated pressure to depend on the atmospheric pressure. Depending on the exit-to-ambient pressure ratio, the base pressure can contribute to a base drag or a base thrust. Base drag can be reduced or eliminated by base bleed [17].

There are two general forms of the aerospike nozzle as shown in Figure 2.3. The linear aerospike nozzle expands its flow in a two-dimensional (2-D) fashion, while the annular aerospike nozzle produces an axisymmetrical flow expansion.

Figure 2.3: Liquid Fuel Linear and Annular Aerospike Engine Testing [18, 19].

In comparing the aerospike and bell nozzles in Figures 2.1 and 2.2, one of the main differences between them is the location of the throat. For a bell shaped nozzle, the throat is located on the center line axis and is relatively easy to manufacture and keep cool during rocket engine firing. This is because there is more space for thermal mass or coolant tubes around the throat. However, for an aerospike nozzle, the throat is located at the outer edge of the contour, where precise manufacturing is required and heat transfer becomes a problem during engine operations. To alleviate the manufacturing and heat transfer problems of an annular aerospike throat, multiple individual modules or thrusters can be placed along or around the spike contour as is the case with both aerospike engines shown in Figure 2.3.

2.2 RPNCC System Concept

The RPNCC approach (Figure 1.7) is a CCP system that provides the potential to improve operational characteristics, improve packaging, and increase performance over the conventional configurations described in Figures 1.1-1.6. By integrating the

aerospike nozzle thrusters into the airbreather nozzle skirt near the exhaust, substantial improvements in performance, cost, and weight can be achieved while reducing complexity. In principle, the RPNCC design allows the rocket engine and the airbreather engine to be independently optimized and operated without the additional complexities and losses in performance associated with the conventional RBCC configuration. This approach further makes the RPNCC engines more accessible, easily refurbished, inspected, and removed/replaced.

The RPNCC configuration incorporates the performance increasing effects of the altitude compensating aerospike nozzle while using the exhaust from the internal airbreathing core to provide the pressurization in the base region as shown in Figure 2.4. The rocket and airbreathing engine exhaust flows only interact at, and downstream of, the aerospike base. This approach avoids the complexity of changing the geometry and locations of the fuel injectors and burners within the ramjet/scramjet ejector.

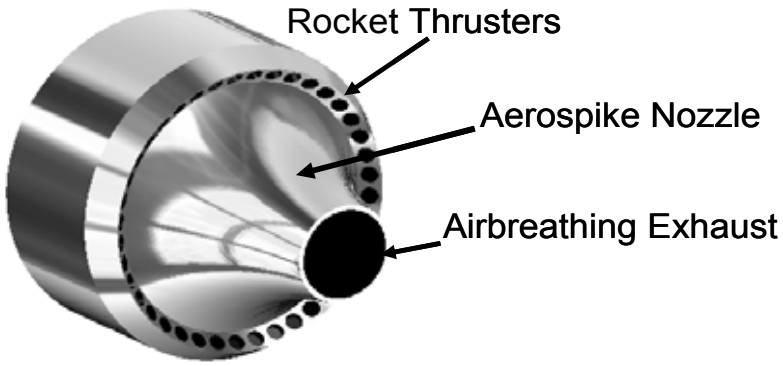

Figure 2.4: RPNCC Nozzle Configuration.

Another advantage of the RPNCC concept is that the plug nozzle thrusters are integrated into the nozzle region which reduces additional cross-sectional area and thus

vehicle drag. This improvement is achieved by taking advantage of the shape of the airbreathing exhaust nozzle configuration to integrate the aerospike thruster engines. Further improvement in performance can be obtained by matching, to the extent feasible, the rocket and airbreathing engine flow velocities and pressures at the exit of the aerospike ramp and internal nozzle, while minimizing the angular changes in the flow field that produce shock interaction losses.

The RPNCC engine could be applied in the same variety of applications as conventional combined cycle propulsion systems. It offers the capability to quickly augment airbreathing engine thrust by turning on or throttling the rocket system and it facilitates a smooth transition between the different propulsion modes throughout the flight regimes. A fundamental advantage of the RPNCC approach is that it would allow parallel and concurrent development of the aerospike rocket and core airbreathing engine systems, rather than the more complex, lengthier, and higher cost iterative development of conventional RBCC systems. This approach could provide earlier system availability, reduce production cost, increase operability, and decrease maintenance costs relative to comparative RBCC systems.

2.3 Preliminary Investigation of the RPNCC Concept

In an early conceptual comparison, both rocket and RPNCC-powered vehicles were used to fulfill the Air Force's Prompt Global Strike Common Aerial Vehicle (CAV) requirements, later designated under the Falcon Program by the Defense Advanced Research Program Agency (DARPA) [20]. Delivery missions were simulated for both RBCC and RPNCC propulsion configurations using the Lockheed developed FASTPASS

multidisciplinary design tool [21]. This analysis showed the vehicle using the RPNCC propulsion system was able to accomplish the same mission with a 23% smaller gross lift-off weight than the conventional rocket-powered system baseline. This was primarily due to the higher efficiency of the aerospike rocket nozzle and simpler airbreathing cruise engine [5].

Preliminary studies consisted of computational fluid dynamic (CFD) simulations of the fundamental physics of the interacting exhaust plumes in the RPNCC nozzle configuration. These simulations were run with the STAR-CCM+ code on a standard personal workstation. Each CFD simulation took over eight hours to run. As mentioned previously, this is much too long for use as part of a vehicle design and optimization process. But these CFD simulations provided relevant data on the plume interactions to justify further investigation and systems studies.

Non-reacting air was used as the working gas in the axisymmetric CFD simulation to see if the combined performance of an airbreathing and aerospike rocket nozzle would be affected by the plume interactions. This situation would occur when transitioning between propulsive modes by increasing one engine's combustion chamber pressure and decreasing the other. By changing the aerospike's Nozzle Pressure Ratio (NPR), which is the combustion chamber pressure to the atmospheric pressure ratio, the rocket engine can be throttled to give a desired exit pressure to match the airbreather or the rocket can be throttled down for airbreather transition.

All the simulations were made with an external flow representing a flight speed of Mach 2.5 at approximately 45,000 feet, which is typically where a conventional RBCC propulsion system would make its transition from an augmented airbreathing-rocket to

pure airbreathing mode for more efficient cruise. The maximum chamber pressures were set to approximately 1000 pounds per square inch (psi) and 150 psi for the aerospike and the airbreather, respectively. Two sets of cases were run. In the first, the NPR and thus thrust of the airbreather was kept at 100% of its maximum value, while the thrust of the aerospike was set to 100%, 75%, 50%, 25%, and 0% of its maximum value by varying the associated NPR of the thrusters. In the second run, the thrust of the aerospike was kept constant while the airbreather thrust was varied. A non-dimensional performance factor was developed by dividing the thrust of the combined nozzle configuration ($T_{aerospike} + T_{airbreather}$) by the sum of the thrust of each component computed independently. If there were no interaction between the aerospike nozzle and the airbreather, this parameter would equal unity.

Preliminary results showed that the airbreather flow does not influence the aerospike nozzle performance even for low aerospike thrust levels. The aerospike flow does not affect the airbreather flow for airbreather thrust level of 100%, 75%, and 50%. However, at 25% airbreather thrust, the flow separated in a very small region near the nozzle wall and the exit plane of the inner nozzle as can be seen in the Mach number plot of Figure 2.5. Similar results were observed in past wind tunnel experiments where boattail missile geometries with an internal jet did not exhibit any reduction in overall thrust of the system [22]. This flow separation occurs for higher values of the aerospike NPR. It was found that the flow interference could be reduced or eliminated by matching the aerospike exit pressure to the exit pressure of the airbreathing nozzle. This is achieved by reducing the aerospike NPR, while increasing the airbreather NPR.

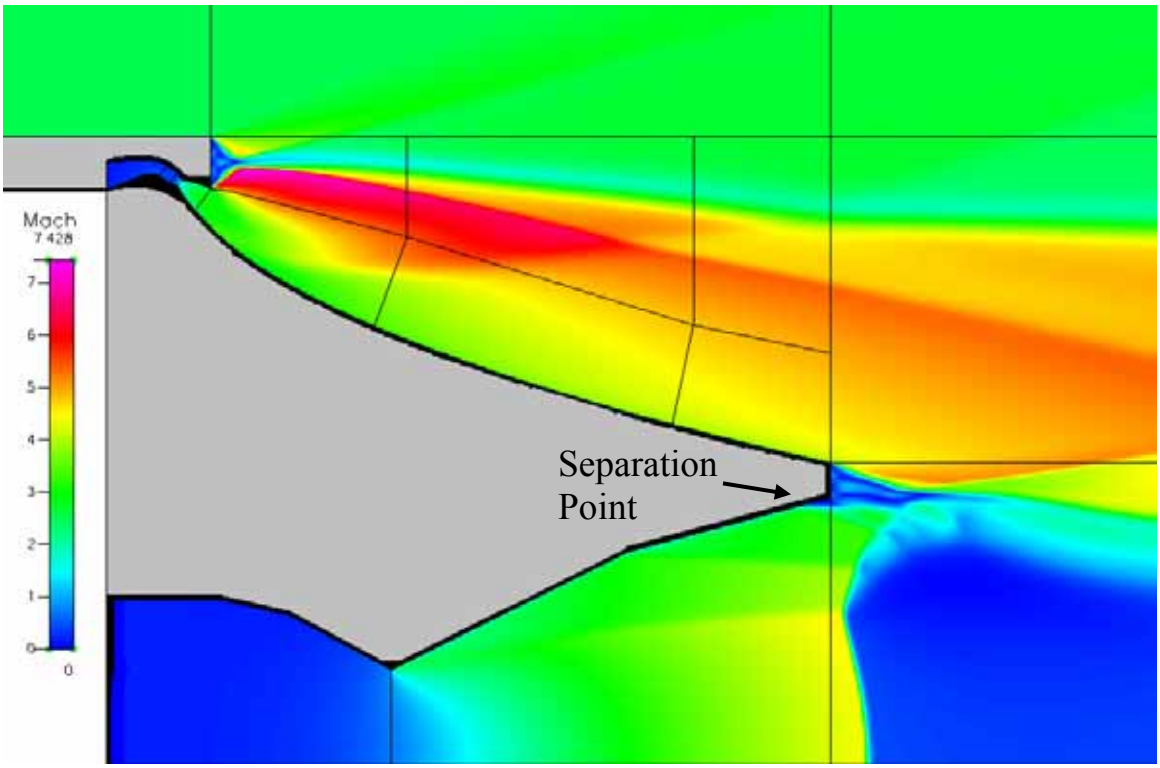

Figure 2.5: CFD predicted Mach number distribution for aerospike thrust at 100% and airbreather thrust at 25%.

The Mach number plot in Figure 2.6 shows the interactions between the ambient freestream flow and the plumes of both engines at maximum chamber pressures for the aerospike and the airbreather. The under-expanded flow at the exit of the aerospike thrusters expands slightly at the exit of the cowl lip and is then immediately pushed back by the higher pressure of the ambient freestream flow. The same phenomenon occurs with the central airbreather plume. The plume is initially under-expanded at the exit plane, but it is immediately constrained by the higher pressure of the aerospike flow on the plug base preventing further expansion. This supersonic flow interaction creates a series of oblique and normal shocks, and Prandtl-Meyer expansion waves. These waves cause the compression and expansions within the plume to form the centralized normal

shock, known as a Mach disk, in the exhaust plume of Figure 2.6. This phenomenon is analogous to the forming of the shock diamonds and a Mach disk observed in the plume of the Space Shuttle Main Engine operating at sea level [23].

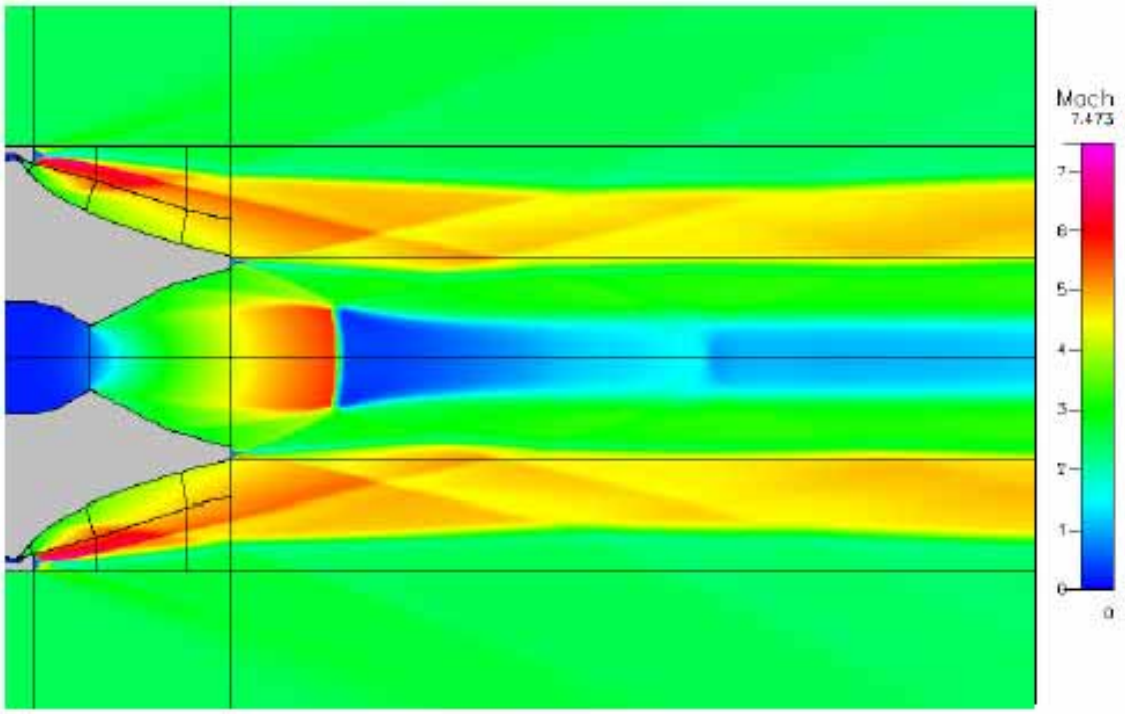

Figure 2.6: CFD predicted Mach number distribution for aerospike thrust at 100% and airbreather thrust at 100% [11].

Results from the preliminary CFD study showed no observable flow of the airbreather gases onto the aerospike ramp or penetration of the rocket nozzle plume into the airbreather nozzle. At these conditions the airbreather and aerospike nozzle essentially operate independently. These results indicate the RPNCC approach could substantially increase the performance of combined cycle propulsion systems and justified further investigation.

CHAPTER 3

NOZZLE PERFORMANCE AND ANALYSIS

3.1 Aerospike Design and Performance Tool

The analysis and optimization of the RPNCC propulsion system and vehicle designs incorporating this new configuration require relatively faster computational tools than CFD. A single case of the prior CFD analysis presented in Chapter 2 requires eight hours to converge on a personal desktop computer. Also, the CFD resources currently available on a single workstation cannot model base flow with enough fidelity to use in the detailed analysis of a design. Thus, the large number of CFD solutions needed is prohibitively expensive and time consuming. Therefore, the Aerospike Design and Performance Tool (ADAPT) [12] was chosen based on its faster analytical capabilities with reasonable model fidelity. The ADAPT code is capable of predicting in a single execution the performance of ten different thruster designs, ten different aerospike contours, and up to ten different off design pressures or NPR values. This allows approximately a thousand different cases to be run in a fraction of the time that it would take to run a single case with CFD.

ADAPT is a collection of existing, proven stand-alone tools linked together to form an integrated analysis tool. The code predicts performance for several types of

altitude compensating rocket engine nozzles including linear, annular, and clustered thruster aerospike nozzles. ADAPT can be used in concert with other analysis techniques to optimize aerospike nozzles over an entire flight envelope. Figure 3.1 shows the individual stand-alone codes used by ADAPT to design and optimize an aerospike nozzle and calculate its performance based on a single user defined input file. The ADAPT code creates input files for each of the sub-codes so that user intervention is not required after the user input file is read. The output is printed to a summary file, which includes the spike and thruster contours, and performance data at each NPR value.

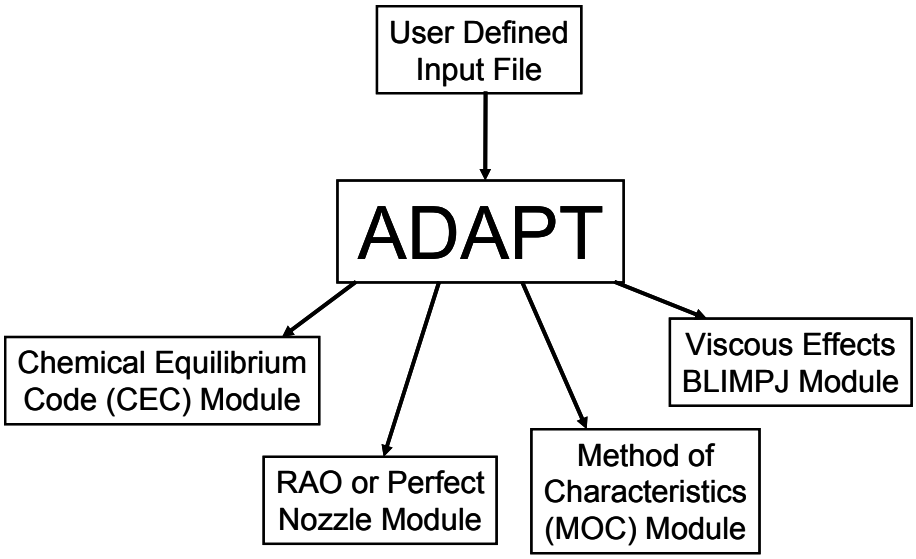

Figure 3.1: ADAPT Logical Structure.

The individual stand-alone tools comprising ADAPT are legacy FORTRAN programs that include the Chemical Equilibrium Code (CEC) [24], the RAO and PERFECT Nozzle codes [25, 26], a method of characteristics (MOC) code [27], and the Boundary Layer Model or BLIMPJ code [28]. The combination of these individual codes

allows ADAPT to save on computational time, giving it the advantage over CFD in the analysis and optimization process.

The ADAPT code is run in four main steps, where each step uses the above legacy programs to calculate parameters needed by the other programs so that information is exchanged without user intervention. The thrusters, i.e., individual module contours, can be designed using one of three choices: the RAO nozzle method [14], which allows for a maximum thrust contour for a specified length and NPR; the PERFECT nozzle method, which by definition turns the exhaust gases parallel and uniform at a specified Mach number and area-ratio; or a User Defined geometry, which allows for a non-ideal contour shape, such as a conical nozzle. This allows ADAPT to analyze both ideal and non-ideal geometries to explore packaging options.

There are two chemical reaction options available in ADAPT. One option is based on ideal gas with a constant ratio of specific heats, γ. This option works well for cold gas analysis, like air, but it typically gives higher temperature results than reality when used for hot gas flows. A real gas chemistry option is available by calling the CEC module to generate the exhaust gas properties and variable ratios of specific heats, which are then used to calculate the isentropic properties at the thruster's sonic line. The real gas option will typically give better results for the aerospike contour construction and calculations of performance parameters for hot flow using actual propellants. For real gas calculations, the reactants data must be specified in the input file.

As discussed in an earlier chapter, the MOC code includes an external expansion method [29] that draws the aerospike contour for isentropic expansion and aligns the thruster exhaust angle measured from the cowl lip with the flow angle of the aerospike

contour. The exit Mach line of the thruster modules and the aerospike nozzle thus coincide. The inside lip of the thruster module is intersected with the point on the aerospike contour that has the same flow angle. The aerospike contour is then translated so that there are no discontinuities between the thruster lip and the isentropic contour [12]. The MOC code calculates the performance and flow field properties of the thruster and aerospike contours.

The BLIMPJ code calculates the viscous losses along the contour of the individual thrusters and aerospike ramp and applies those losses to the overall performance analysis. A performance summary output file is written along with output files of the two-dimensional contour of the plug and thruster geometries, and a summary of thruster and plug contour flow field properties. For a detailed description of the input files required by ADAPT and the specific output files produced, the reader is referenced to Smith [12] and Higdon [30].

3.2 ADAPT Validation

Previous modifications to the original ADAPT source code included adding a subroutine that accounts for incomplete combustion and heat losses, which results in a lower combustion efficiency, C*, than theory predicts [12]; several base pressure calculation methods for truncated spikes without base bleed conditions [31]; and the capability to analyze both ideal and non-ideal contour geometry [12, 30]. The base pressure correlations used in ADAPT are strictly for the no base bleed condition and when the aerospike is operating at or above its design NPR or closed base-wake conditions [31].

In a previous validation study, ADAPT was shown to compare very well to experimental wind tunnel data and CFD predictions [30]. CFD simulations from NASA Marshall Space Flight Center (MSFC) and the Technical University of Dresdan (TU Delft) of a plug nozzle run at different NPR values were compared to data from a linear aerospike wind tunnel experiment [30]. Figure 3.2 shows excellent agreement between the ADAPT results and the experimental data. Similar results are also seen in comparisons to additional annular aerospike wind tunnel tests performed at NASA MSFC [30].

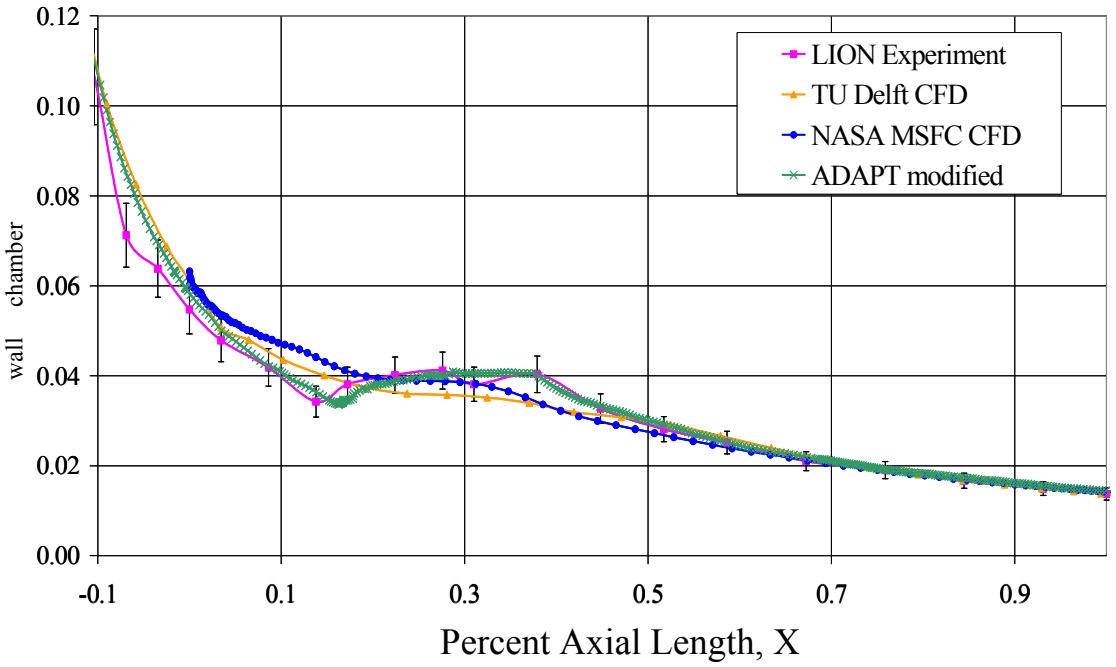

Figure 3.2: Wind tunnel experiment and CFD compared to ADAPT [30]
(Reprinted by permission.)

3.3 Required ADAPT Changes for Base Pressure Calculations

While the previously modified version of ADAPT was capable of designing and predicting aerospike rocket performance, it could not model an airbreathing core in the base of the aerospike nozzle. The code is capable of performing the calculations and design optimization for both a conventional bell-rocket nozzle and an aerospike nozzle separately, but not together, i.e., with the exhaust plumes flowing co-axially. Also, the flow field calculations from the MOC code stop at the base of the aerospike and/or exit of the bell-nozzle. It is not required to know what happens to the exhaust gases and plume interactions after the exit plane of the nozzle beyond estimating a base pressure value for the net thrust calculation. However, by adding an airbreathing core to pressurize the base region of the truncated plug nozzle, base bleed effects must be introduced to the base pressure and net thrust calculations. As mentioned before, the built-in base pressure models in ADAPT for a truncated aerospike are only for no-base-bleed conditions. Therefore, a base pressure correlation to model the base bleed conditions as the airbreather's NPR increases during engine mode transitions is needed to determine the base-lip pressure between the exit of the aerospike ramp and the exit of the internal airbreathing nozzle. These base-lip pressures are needed for a more accurate net thrust calculation during performance analysis.

By assuming a similar geometrical relation to a boattail afterbody with jet-on effects, a modified empirical approach for estimating the base pressure of bodies of revolution with a central jet exhausting through the base can be used to estimate the base-lip pressure. By this logic the aerospike rocket flow is analogous to the ambient freestream flow over a boattail afterbody and the internal airbreather flow is similar to the

flow exhausting from the centralized jet. This modification to the base pressure calculation was added to ADAPT in a subroutine to the main code and can be used to determine performance data for conceptual flight vehicle design studies using this particular plug nozzle configuration. A description of the base pressure correlation, the assumptions and methodology in applying it to an aerospike nozzle, and validation of the method are the basis of the next chapter.

CHAPTER 4

BASE PRESSURE MODELS

4.1 Experimental Base Pressure Technique

With the advent of computational fluid dynamics (CFD) and ever-evolving analytical and empirical techniques, the capability to predict base pressure has evolved to more sophisticated techniques over the past few decades. But even with CFD and some of the more advanced empirical and theoretical base pressure correlations, it still remains an elusive problem to accurately predict base pressures for more than specific geometries and flight conditions. For quick and relatively accurate analytical analysis of a flight vehicle or propulsion system, CFD does not provide for a suitable solution within time and financial limitations. On the other hand, empirical correlations that take into account most geometric and propulsive aspects like boattails, flares, high and low thrust, transonic as well as high supersonic freestream conditions, etc., are usually too inclusive to give accurate results because the data is too scattered across so many different flow regimes. It is for these reasons that a general empirical method tailored to a more specific geometric flight vehicle and propulsion system was needed to predict base pressures for the RPNCC system and performance analysis.

The empirical approach discussed in this thesis was first correlated by Brazzel and Henderson [32] in the mid 1960's with an assortment of experimental wind tunnel data from several different NACA and U.S. Army Missile wind tunnel facilities. The majority of the data was taken at supersonic freestream speeds using a single or double strut mounting configuration for the wind tunnel model [33, 34, 35, 36, 37]. All the models had a hollow internal nozzle. Pressurized air was fed through the mounting strut to analyze jet-on effects on base pressure for various jet parameters, such as Jet Mach number, Pressure, Nozzle exit deflection angle, etc., and freestream Mach numbers. The majority of the models had interchangeable afterbody and/or nozzle sections to study the effects of boattail and nozzle geometries with jet-on conditions.

Figure 4.1 shows the general shapes of the boattail geometries looked at in the wind tunnel experiments. The ogive boattail, created continuous Prandtl-Meyer expansion waves along the surface to the base, which decreased the pressure along the surface of the flight vehicle afterbody. The cusp shaped boattail produced the same initial Prandtl-Meyer expansion wave at the beginning of the boattail. But, the flow along the surface was immediately turned back toward the parallel direction with the freestream flow, which created continuous compression waves along the remainder of the boattail surface to the base and thus ultimately increased the pressure of the freestream along the surface of the flight vehicle afterbody. Several different conical boattail shapes were also studied.

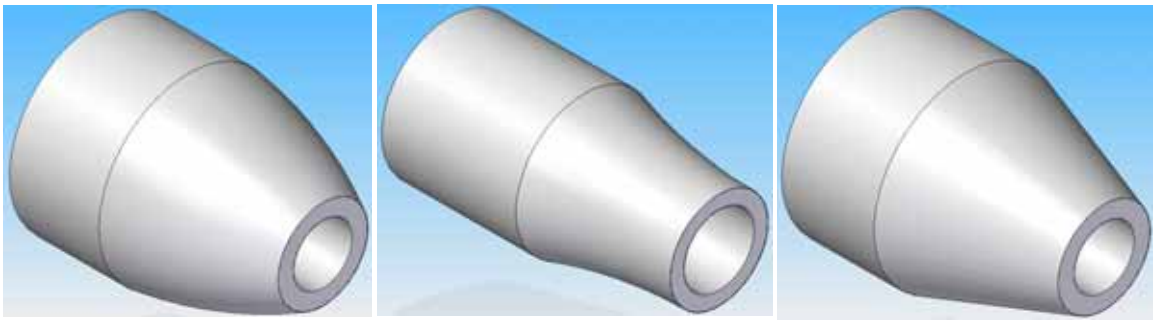

Figure 4.1: General Experimental Afterbody Model Shapes from left to right: Ogive, Cusp, and Conical.

4.2 Factors Affecting Base Pressure

Figure 4.2 shows general geometric and flow parameters for the models used in gathering the experimental base pressure data. Here, d_j is the exit diameter of the jet, d_B is the diameter of the base, d_{ref} is the diameter of the body, and P_B is the base static pressure. The parameters T_j, M_j, P_j, and γ_j are the temperature, Mach number, static pressure, and specific heat ratio at the exit of the inner jet nozzle, respectively. The parameters T_∞, M_∞, P_∞, and γ_∞ are the corresponding freestream conditions.

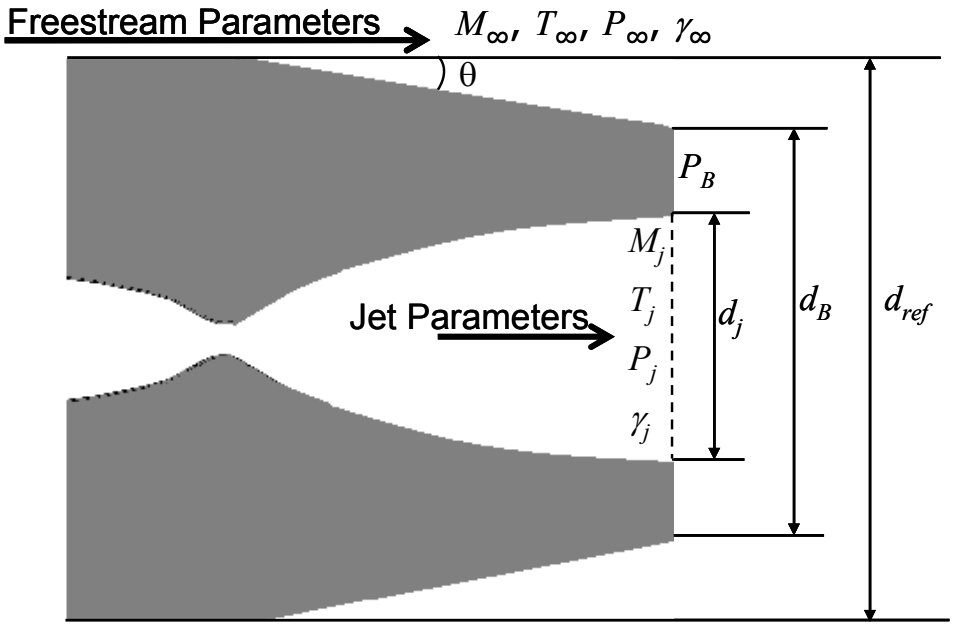

Figure 4.2: General Geometry of Boattailed Afterbody Section of Wind Tunnel Models.

The basis of Brazzel and Henderson's correlation [32] is an apparent relationship between the base pressure ratio, P_B/P_∞, and the ratio of momentum flux of the jet to the momentum flux of the freestream or equivalent body stream-tube (*RMF*). The jet momentum flux ratio is given by

$$RMF = \frac{(\dot{m}V)_j}{(\dot{m}V)_\infty}. \tag{4.1}$$

The mass flow rate is defined by

$$\dot{m} = \rho V A, \tag{4.2}$$

where the perfect gas equation yields the density

$$\rho = \frac{P}{RT}. \tag{4.3}$$

Substituting these definitions and the definition of the speed of sound,

$$a^2 = \gamma RT, \tag{4.4}$$

into the momentum flux yields

$$\dot{m}V = \frac{P}{RT}V^2A = \frac{\gamma}{\gamma}\frac{P}{RT}V^2A = \frac{\gamma PV^2A}{a^2} = \gamma PAM^2. \tag{4.5}$$

Therefore the momentum flux ratio can be rewritten in terms of specific heat ratio, pressure, area and Mach number as

$$RMF = \frac{\gamma_j P_j A_j M_j^2}{\gamma_\infty P_\infty A_\infty M_\infty^2} = \frac{\gamma_j P_j d_j^2 M_j^2}{\gamma_\infty P_\infty d_{ref}^2 M_\infty^2}. \tag{4.6}$$

The momentum flux is the predominant term in the jet thrust equation,

$$Thrust = \left(\dot{m}V\right)_j + A_j\left(P_j - P_\infty\right). \tag{4.7}$$

The freestream momentum flux can be written as,

$$\left(\dot{m}V\right)_\infty = \gamma_\infty P_\infty A_B M_\infty^2 = 2\frac{\gamma_\infty}{2}P_\infty M_\infty^2 A_B = 2q_\infty A_B. \tag{4.8}$$

The thrust coefficient is defined as the thrust normalized by a reference pressure and area term, typically freestream dynamic pressure and the body diameter of a missile, yielding

$$C_T = \frac{Thrust}{q_\infty A_{ref}}. \tag{4.9}$$

Using Equation 4.1 the thrust coefficient definition and mass flux relationships in Equations 4.7, 4.8, and 4.9, and assuming that the jet exit pressure is equal to the ambient pressure, yields the relationship

$$RMF = \frac{(\dot{m}V)_j}{(\dot{m}V)_\infty} \cong \frac{Thrust}{2q_\infty A_{ref}} = \frac{C_T}{2}. \tag{4.10}$$

The base pressure correlation in Brazzel's original method is defined as

$$\frac{P_B}{P_\infty} = \left[\frac{T_j}{T_j^*}\right]\left[C_1 + C_2\left(\frac{RMF}{1+RMF}\right)\right]\left[\frac{3.5}{1+2.5\left(A_B/A_{ref}\right)}\right] + 0.047\left(5 - M_\infty\right)\left[2\left(\frac{x_j}{d_B}\right) + \left(\frac{x_j}{d_B}\right)^2\right], \tag{4.11}$$

where $C_1 = 0.19$ and $C_2 = 1.28$. The first bracketed term on the right hand side of Equation 4.11 is the ratio of static temperatures. Brazzel and Henderson [32] found that for all jet Mach numbers, the base pressures are proportional, regardless of thrust level, and that the proportionality factor is closely related to the jet temperatures. One of the significant assumptions of the Brazzel method is that the jet exit Mach number can be described by a ratio of the jet static temperature at a given jet Mach number to the static temperature at a jet exit Mach number of one [38]. This relation is illustrated by the temperature ratio equation,

$$\frac{T_j}{T_j^*} = \frac{\frac{\gamma_j + 1}{2}}{1 + \frac{\gamma_j - 1}{2} M_j^2}. \tag{4.12}$$

The effects of stagnation temperature and the ratio of specific heats were not experimentally analyzed, but theoretical investigations developed by Korst [39] showed that these parameters had extremely small influence on base pressure [32].

The second bracketed term on the right side of Equation 4.11 is the momentum flux relation, which expresses how the base pressure ratio varies with the jet momentum flux ratio. The two leading coefficients were initially determined for a lower range of thrust coefficient between about 0.08 and 3.0 [38]. This thrust coefficient range typically corresponds to sustainer levels of thrust, like a loitering airbreathing engine. This term is also where the free stream Mach number, nozzle diameter, and divergence angle are accounted for in Equation 4.11.

The third bracketed term on the right hand side of Equation 4.11 is related to non-cylindrical afterbody geometry, i.e., boattail and flare effects on the base pressure. This term is a linear approximation of both boattail and flare afterbody experimental data for base-to-body diameter ratios, d_B/d_{ref}, from 0.416 to 1.533,

$$\left(\frac{P_B}{P_\infty}\right)_{NON-CYL} = \left(\frac{P_B}{P_\infty}\right)_{CYL} \left[\frac{3.5}{1 + 2.5\left(A_B / A_{ref}\right)}\right]. \tag{4.13}$$

In Equation 4.13, there appears to be a slight discontinuity between boattail and flare values of the ratio of base pressures of cylindrical bodies to non-cylindrical bodies or the proportionality factor ($P_{B\_CYL}/P_{B\_NON\text{-}CYL}$). This is not an issue here, because it is

only necessary to model the boattail effects to relate to the aerospike ramp on the RPNCC configuration. It will be discussed in a later section how the data for flares was therefore ignored and a better linear approximation was developed for boattail and cylindrical afterbody geometries only.

Brazzel et al. [32] noted that the experimental data used to correlate Equation 4.13 is based on tests that incorporated several different boattail angles and lengths as well as different base-to-jet diameter ratios. Therefore, it is believed that the empirical correlation accounts for the different boattail geometrical effects relatively accurately. Furthermore, Rubin et al. [35] found that the primary influence of boattail geometry is due to base diameter or the base-to-jet diameter ratio, d_B/d_j, and not as much on boattail angle, θ, or length, L_b. For a constant base-to-body diameter ratio the length of the boattail will increase for decreasing boattail angle. Figure 4.3 shows that despite different boattail angles and corresponding lengths, for a given base diameter, the base pressure is relatively constant.

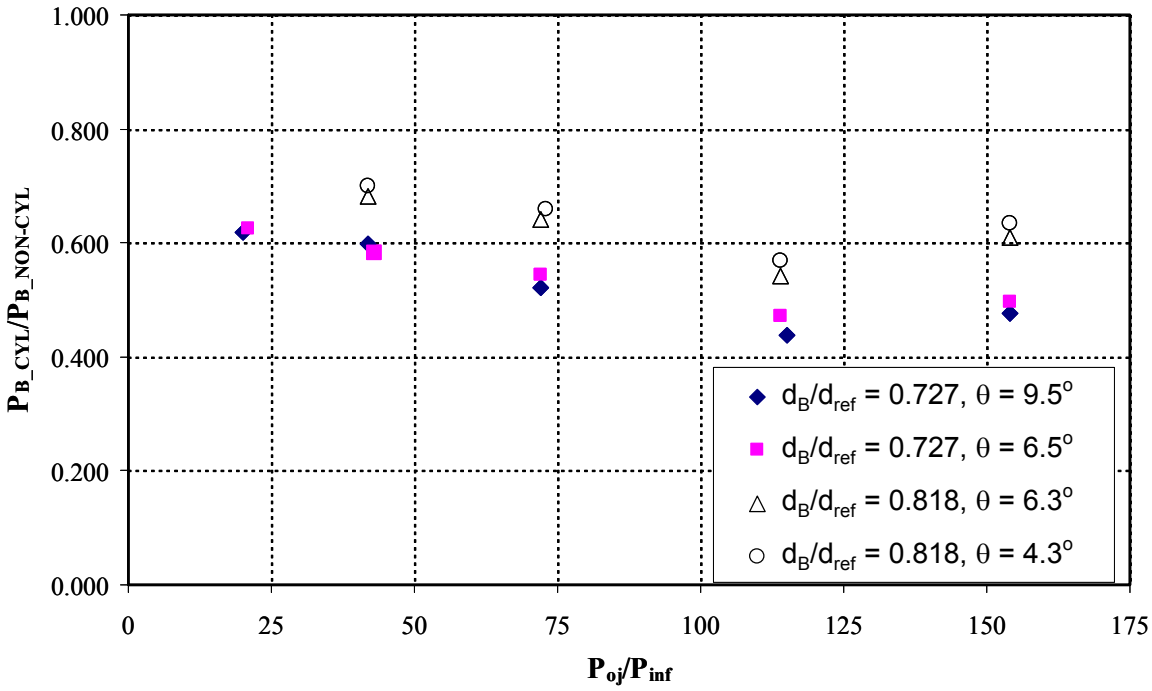

Figure 4.3: Proportionality Factor as a Function of NPR [35].

Figure 4.4 shows the same boattail geometries used in Figure 4.3 versus a cylindrical afterbody with a boattail angle of zero. It can be seen that the base pressure ratio, P_B/P_∞, changes very little with boattail angle and length, but does change with base diameter. It is also interesting to note the relation of NPR with base pressure. In Figure 4.4 the base pressure is at its maximum when the jet flow becomes choked or sonic. The base pressure decreases from this maximum until the exit pressure of the jet equals the base pressure as seen by the dip in the curves. As the NPR continues to increase, the exit pressure begins to exceed the base pressure and an expansion fan forms at the exit-edge of the jet nozzle. The jet nozzle becomes under-expanded, and the base pressure begins to rise with increasing NPR. From the experimental data from

Rubin et al. [35] and Figures 4.3 and 4.4, it is assumed that boattail angle and length play a relatively negligible role in determining the base pressure of bodies of revolution.

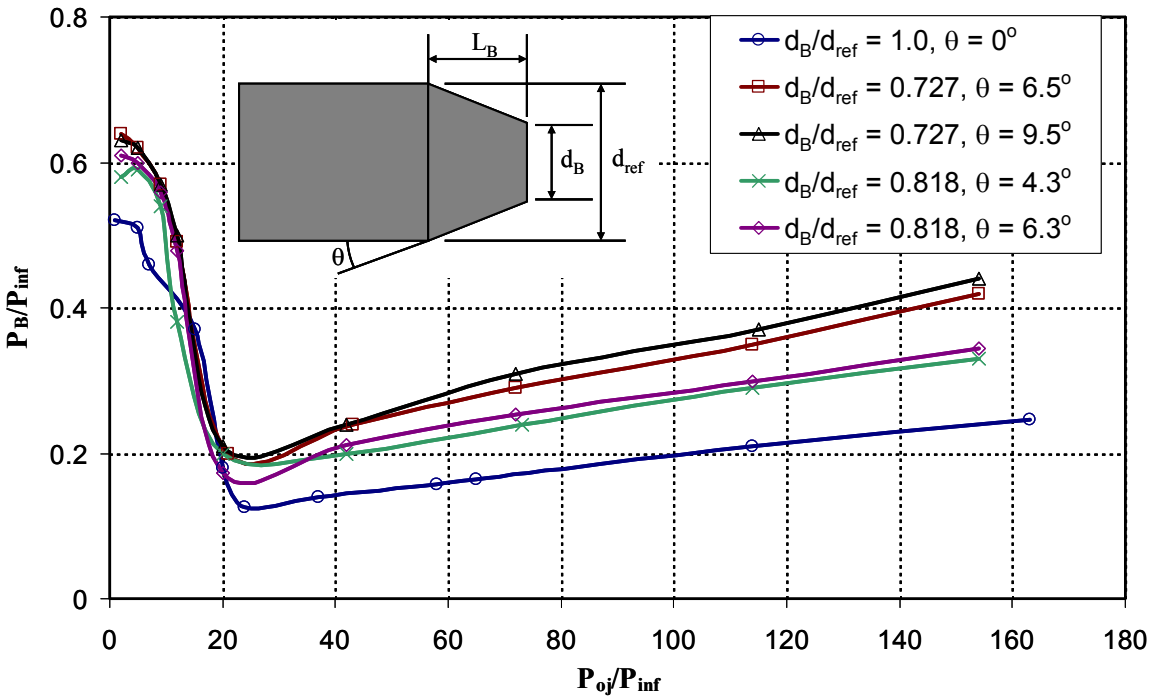

Figure 4.4: Effects of Boattail Geometry on Base Pressure [35].

The fourth bracketed term on the right hand side of Equation 4.11 is the effect of nozzle exit position relative to the base of the afterbody. It is merely a function of nozzle position, nozzle diameter, and free stream Mach number, and it is independent of thrust coefficient. This term was set to zero for the RPNCC configuration because the internal nozzle is assumed flush with the base of the aerospike nozzle.

The boundary layer over the body is generally considered to exert a considerable influence on base pressure and it is thought that the viscous effects are responsible for a small amount of scatter in the data which was used to correlate Equation 4.11. However,

the empirical expression formulated by Brazzel and Henderson [32] includes the major influences of body boundary layer effects from experimental wind tunnel data. Therefore, it is felt that the viscous effects are accounted for and no extra expression is required in the correlation.

Experimental data showed that for nozzle diameter to reference diameter ratios, d_j/d_{ref}, of 0.65 and higher, i.e., for larger nozzle exit diameter and smaller base-lip area, the nozzle exit angle had significant influences on base pressure [33, 34, 35]. However, for lower nozzle diameter ratios, the nozzle exit angle had little effect on base pressure and was considered negligible [36, 37]. This trend is also seen in the theoretical correlation developed by Korst [39]. Brazzel et al. [32] noted that for the larger nozzle exit diameters, the resulting base annulus area was small. Combining this with the high thrust from a larger nozzle yielded a considerably higher base pressure and a lower base drag coefficient. This trend was seen throughout the experimental data used to develop this correlation and therefore is not believed to significantly influence the base pressure prediction [32].

Brazzel also showed that nozzle diameter has very little effect on base pressure when plotted as a function of the *RMF*. However, nozzle diameter for geometrically similar nozzles does influence the base drag because it is a function of both base pressure and annulus area [32].

Although the majority of the data used in the Brazzel correlation is from cold-air jets, there were a few hot-gas tests with propane and oxygen [33] and the relation has shown relatively good agreement with some smaller sustainer motor firings. It is, therefore, believed to serve as a good preliminary method for determining base pressure.

The advantage of using Brazzel's method is in the speed and ease of its use. Even though its prediction error can in some cases be on the order of 15%, this is still within "engineering accuracy."

The major drawback of Brazzel's method, as noted by Moore [38], is its limitation outside its associated *RMF* range. As can be seen in Figure 4.5, the Brazzel method is relatively accurate below *RMF* values of 1.5. But, above this value the experimental data becomes much more scattered and the method of Brazzel is less accurate. This is primarily due to the two leading coefficients ($C_1 = 0.19$, $C_2 = 1.28$), in the *RMF* bracketed term of Equation 4.11, being outside the range of applicable experimental data. However, Moore [38] developed a table of multiple values for (C_1, C_2) based on higher levels of thrust coefficients typical of booster motors. The other curves in Figure 4.5 are the Brazzel's correlation based on higher thrust levels using Moore's coefficients.

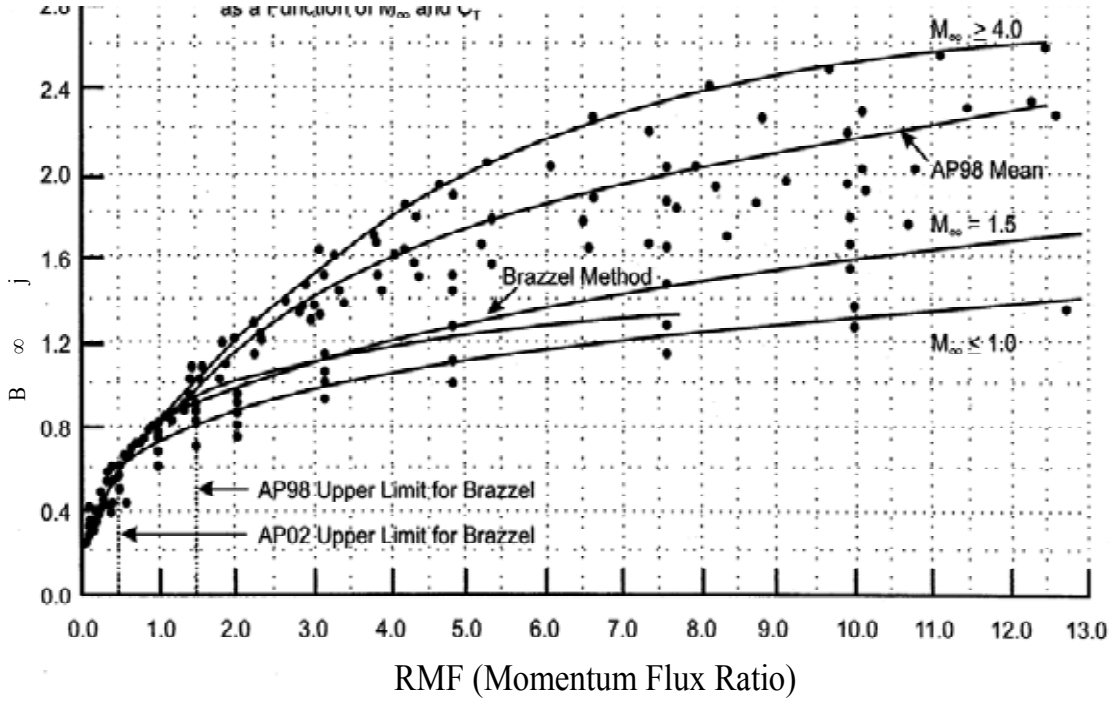

Figure 4.5: Base Pressure as a Function of Momentum Flux Ratio for a Cylindrical Afterbody with jet exit Mach number of unity [38].
(Reprinted by Permission.)

In Equation 4.10, thrust, atmospheric pressure, freestream Mach number, and the vehicle cross section are key figures of merit when estimating the *RMF* to determine the validity of the leading coefficients in Brazzel's method for certain flight scenarios. For example, the Brazzel's method starts to become inaccurate for thrust levels of 25,000 pound force (lbf) at altitudes above 65,000 feet, Mach numbers below four and flight vehicle diameters of less than three feet. It will be shown, however, in the following example that for the purpose of this thesis and preliminary analysis, Brazzel's original C_1 and C_2 values are sufficient in determining base pressure for the RPNCC configuration.

The Talos Missile [8, 9] and its associated mission were chosen to assess whether the *RMF* values would be in the appropriate range for a preliminary RPNCC analysis. An average altitude of 50,000 feet was chosen for the transition of the engine modes, which is where the airbreather will power cruising flight without rocket assisted thrust. When the aerospike thrusters have turned off, the aerospike ramp will be analogous to a boattail on the flight vehicle and the aft geometry can be treated as such, with the freestream flow parameters over the forebody in Equation 4.11. The airbreather is given a thrust value of about 21,000 lbf, which is comparable to the sustainer thrust produced by the Talos missile [8, 9]. A flight vehicle about 2.0 feet in diameter cruising at 50,000 feet and Mach 3.0, and assuming the ramjet nozzle is designed for 50,000 feet, yields reasonable *RMF* value of about 0.63, which is in the limits of the Brazzel's method given by Equation 4.11. Thus, for sustainer thrust levels lower than 21,000 lbf and altitudes below 50,000 feet, there should not be any reason to include Moore's methodology for higher values of *RMF* for preliminary analysis.

In the cases that high altitudes and thrust levels need to be analyzed, where *RMF* values are higher or outside the limits of Brazzel's original coefficients, Moore's table of leading coefficients can be used to give better results of base pressures. For the purpose of this study, however, Moore's coefficients were not needed because the typical airbreather in a cruise missile configuration is only capable of sustaining thrust levels and is not used as the main accelerative force beyond its supersonic cruise capabilities [8, 9]. So, it is beyond the scope of this thesis to investigate the base pressure correlation for higher thrust levels or higher values of *RMF*.

It is assumed that the RPNCC configuration is similar in form to the physical wind tunnel models used in gathering data for the empirical base pressure correlation and that it will provide a good estimate of base-lip pressure for a first order analysis of the net thrust and performance characteristics of this type of configuration with relatively good engineering accuracy. It can also be assumed that because the aerospike ramp is similar to the boattail geometry the aerospike rocket exhaust parameters can be used as the freestream parameters in Equation 4.11 during aerospike operation. This will determine the base-lip pressure for net thrust calculations in the boost and transitional phases of flight. To demonstrate this concept Figure 4.6 shows the corresponding geometric and flow parameters for the RPNCC nozzle configuration. Here, d_j is the exit diameter of the inner nozzle, d_B is the aerospike base diameter, and P_B is the base-lip static pressure. The parameters T_j, M_j, P_j, and γ_j are the exit conditions of the inner nozzle and T_∞, M_∞, P_∞, and γ_∞ are the aerospike flow conditions.

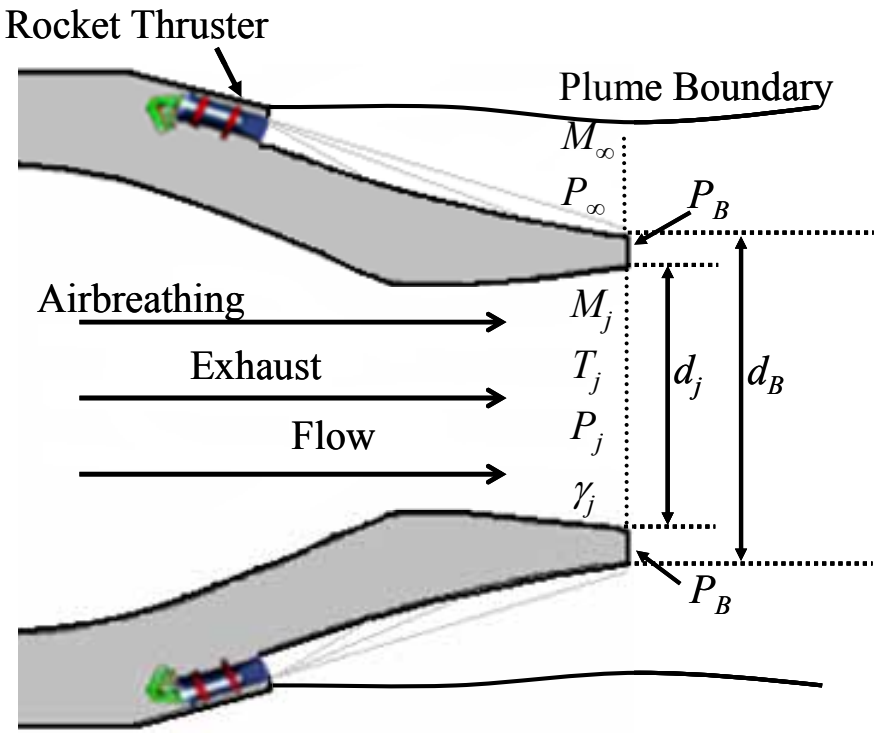

Figure 4.6: Geometrical Parameters of RPNCC Nozzle and Base-lip Pressure Parameters.

In the simplest approach, the inner airbreather jet momentum flux (*RMF*) ratio can be calculated using one-dimensional flow equations and assuming no losses in the nozzle. A more exact approach would be to calculate the property distributions at the exit plane of the internal jet nozzle and corresponding external aerospike nozzles properties using the MOC, CEC, and BLIMPJ codes in ADAPT. At first glance it appears that the ambient flow values, designated by the ∞ subscript in Equations 4.6 and 4.11, are determined by averaging the corresponding parameter values across the aerospike plume exit plane at the end of the ramp and using the aerospike base diameter as the reference diameter. This corresponds to assuming simple cylindrical afterbody geometry when using the empirical correlation in Equation 4.11. However, it will be discussed in a later section that this assumption is not geometrically or physically justified for the particular

flow configuration of the RPNCC. On the other hand, the internal jet parameters are determined by averaging the corresponding parameter values across the inner jet nozzle exit plane, like they were for the majority of the wind tunnel experiments [33, 34, 35, 36, 37].

In summary, the empirical correlation (Equation 4.11) is used to estimate the base-lip pressure between the aerospike and internal nozzle for net thrust and performance calculations. To do this it is assumed that the aerospike flow will act as the freestream flow during aerospike operations. The freestream over the forebody is used for no-aerospike operations. Therefore, Equation 4.11 can be used to estimate the base-lip pressure as it would for the base region of conventional cylindrical and boattail missiles. The reader is also reminded that despite the thrust level of the aerospike rocket nozzle, it is the exit Mach number and pressure of the rocket exhaust that are the important factors and as long as the *RMF* ratio is below 1.5, the leading coefficients in Equation 4.11 are applicable.

The following sections describe how Equation 4.13 and consequently Equation 4.11 were modified to model boattail geometry more closely, how the reference parameters were chosen, and how to handle the "no-jet" and base bleed effects for extremely low *RMF* values.

4.3 Boattail Geometry Factor

As discussed earlier, a new linear approximation was developed by ignoring the flare data used to develop Equation 4.13. Only the boattail and cylindrical data from Baughman et al. [33], Cortright et al. [34], and Rubin et al. [35] were used in Figure 4.7.

The new approximation allows for more accurate calculations of boattailed geometries similar to an aerospike nozzle. In Figure 4.7 Brazzel's linear approximation, Equation 4.13, and the new linear approximation for just boattail and cylindrical afterbody geometries are plotted against experimental data [33, 34, 35].

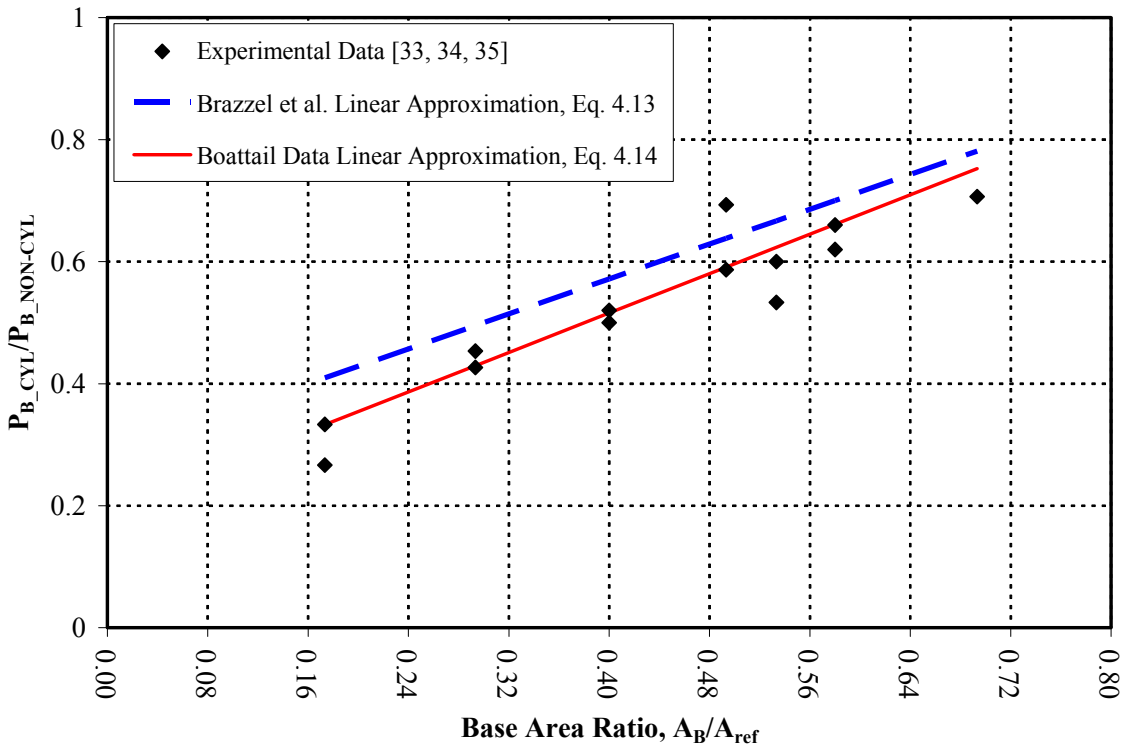

Figure 4.7: Proportionality Factor for Boattail Afterbodies Only as a Function of Base Area Ratio [33, 34, 35].

By analyzing only cylindrical boattail afterbody data, a new linear approximation was defined

$$\left(\frac{P_B}{P_\infty}\right)_{NON-CYL} = \left(\frac{P_B}{P_\infty}\right)_{CYL}\left[\frac{1}{0.1929 + 0.8071\left(A_B/A_{ref}\right)}\right]. \qquad (4.14)$$

Equation 4.14 better captures the influence of base diameter on base pressure for boattail and cylindrical afterbody geometries only. Therefore, a modified base pressure correlation for cylindrical and boattail afterbody geometries with flush nozzles is given by

$$\frac{P_B}{P_\infty} = \left[\frac{T_j}{T_j^*}\right]\left[0.19 + 1.28\left(\frac{RMF}{1+RMF}\right)\right]\left[\frac{1}{0.1929 + 0.8071\left(A_B/A_{ref}\right)}\right]. \qquad (4.15)$$

This approximation is compared to data in Figure 4.7 and the improved accuracy is evident. Tables 4.1 and 4.2 compare experimentally measured base pressure values to predictions made with the original Brazzel correlation (Equation 4.11) and the modified correlation (Equation 4.15) for corresponding values of the *RMF* ratio. The two tables represent the high and low ends of the freestream Mach numbers used throughout the base pressure experiments. Similar comparisons were made with the experimental data from Baughman et al. [33], Cortright et al. [34], and Rubin et al. [35]. These comparisons gave similar results and are not shown for the sake of brevity.

Table 4.1: Comparison of Base Pressure Correlations against Experiment [35] at high freestream Mach number, $M_j = 2.7$.

$M_\infty = 3.5$, $d_B/d_{ref} = 0.818$, $\theta = 6.35^o$						
Experiment P_{oj}/P_∞	**Experiment P_B/P_∞**	**RMF**	**Eqn. 4.11 P_B/P_∞**	**Eqn. 4.15 P_B/P_∞**	**Eqn. 4.11 Error %**	**Eqn. 4.15 Error %**
30	0.180	0.034	0.159	0.163	11.7	9.1
56	0.200	0.064	0.183	0.188	8.6	6.0
115	0.250	0.132	0.232	0.239	7.2	4.5
201	0.290	0.222	0.282	0.291	2.6	0.2
315	0.344	0.335	0.334	0.344	2.8	0.1

Table 4.2: Comparison of Base Pressure Correlations against Experiment [33] at low freestream Mach numbers, $M_j = 2.19$.

$M_\infty = 1.91$, $d_B/d_{ref} = 0.525$, $\theta = 11.0^o$						
Experiment P_{oj}/P_∞	**Experiment P_B/P_∞**	**RMF**	**Eqn. 4.11 P_B/P_∞**	**Eqn. 4.15 P_B/P_∞**	**Eqn. 4.11 Error %**	**Eqn. 4.15 Error %**
6.2	0.653	0.137	0.531	0.588	18.6	9.9
10.7	0.725	0.223	0.611	0.677	15.6	6.6
14.3	0.764	0.281	0.651	0.720	14.9	5.8
26.3	0.943	0.504	0.836	0.926	11.3	1.9

It is seen from Tables 4.1 and 4.2 that the percent errors with the new boattail correlation (Equation 4.15) are relatively smaller than with the original Brazzel correlation (Equation 4.11) against the experimental data. This trend is seen throughout the majority of the experimental data [33, 34, 35] and it is believed that Equation 4.15 will relate more accurately to the geometric assumption of using this empirical method to determine the base-lip pressure of the aerospike and airbreather nozzles in ADAPT.

In Tables 4.1 and 4.2 it can be seen that as the *RMF* decreases the percent error increases. This is due to the limited *RMF* range for low momentum flux data from the inner jet. The base area is physically entering more of a base-bleed state at lower *RMF* values. This phenomenon is discussed in more detail in a later section.

4.4 Defining Freestream Reference

Because ADAPT calculates the Mach number and flow properties at the exit of the aerospike ramp, it was originally thought to use these parameters as the freestream values in Equation 4.11 with the diameter of the base of the aerospike nozzle as the

reference diameter. This corresponds to a cylindrical afterbody geometry assumption, neglecting the boattail term (Equation 4.14) in Equation 4.15. Figure 4.8 shows the general geometry and flow parameters before and after the expansive turning angle of the boattail. The parameters at the end of the aerospike ramp correspond more closely to those at the end of the boattail or station 2 in Figure 4.8 and not the freestream parameters before the expansion at station 1 as assumed with the cylindrical afterbody geometry. This suggested a study of whether freestream parameters should be referenced prior to the flow being turned and expanded, or should they be referenced to the end of the aerospike ramp. In other words, the flow emanating from the individual thruster nozzles around the aerospike ramp corresponds to the freestream flow at station 1 in Figure 4.8, rather than the parameters at the end of the aerospike ramp or boattail at station 2. By using the thruster properties, the flow is referenced before it expands over the spike contour, similar to the freestream over the forebody of a conventional cylindrical missile.

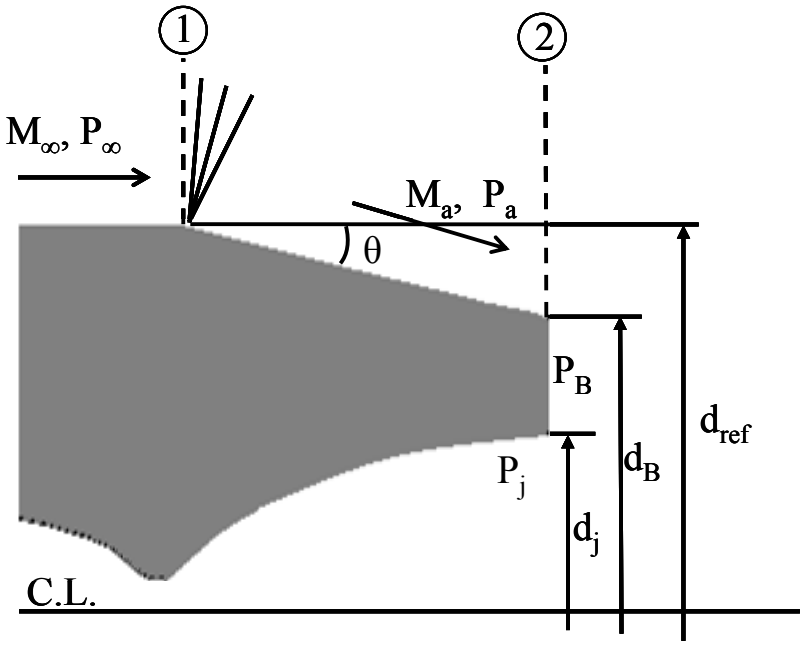

Figure 4.8: Nomenclature of Flow Turning Toward Base through the Boattail Angle.

If using the parameters at the end of the aerospike ramp (station 2 in Figure 4.8), Equation 4.14 would need to be set to unity, which corresponds to a cylindrical afterbody with no boattail. However, if using the parameters at the thruster exit (station 1 before the expansion), the reference diameter and freestream parameters will change and Equation 4.14 will be some finite number that will affect the base pressure.

Experimental data [33, 34] for different boattail geometries were used to estimate the Mach number and boattail pressure ratio at the base of the model. The boattail pressure ratio is the freestream pressure over the forebody to the pressure at the end of the boattail. The parameters at the end of the boattail are designated with the subscript, *a*. By multiplying the jet-to-freestream pressure ratio, P_j/P_∞, by the boattail pressure ratio, the jet-to-boattail pressure ratio, P_j/P_a, can be used to determine the base pressure ratio in Equation 4.15. Prandtl Meyer expansion wave theory [15], given by

$$\nu\left(M_\infty\right)=\sqrt{\frac{\gamma+1}{\gamma-1}}\tan^{-1}\left(\sqrt{\frac{\gamma-1}{\gamma+1}\left(M_\infty^2-1\right)}\right)-\tan^{-1}\left(\sqrt{M_\infty^2-1}\right), \tag{4.16}$$

$$\theta_a=\nu\left(M_a\right)-\nu\left(M_\infty\right), \text{ and} \tag{4.17}$$

$$\frac{P_\infty}{P_a}=\left[\frac{1+\frac{\gamma-1}{2}\left(M_a\right)^2}{1+\frac{\gamma-1}{2}\left(M_\infty\right)^2}\right]^{\gamma/\gamma-1}, \tag{4.18}$$

is used to determine the Mach number and pressure just after the initial boattail turning angle. Oblique shock wave theory [15], given by

$$\tan\left(\theta\right)=2\cot\left(\beta\right)\left[\frac{M_1^2\sin^2\left(\beta\right)-1}{M_1^2\left(\gamma+\cos\left(2\beta\right)\right)+2}\right], \tag{4.19}$$

$$M_{n1}=M_1\sin\left(\beta\right), \tag{4.20}$$

$$M_{n2}^2=\frac{M_{n1}^2+\left[2/\left(\gamma-1\right)\right]}{M_{n1}^2\left[2\gamma/\left(\gamma-1\right)\right]-1}, \text{ and} \tag{4.21}$$

$$M_2=\frac{M_{n2}}{\sin\left(\beta-\theta\right)}, \tag{4.22}$$

is used to determine the Mach number and pressure just after a compression or oblique shock wave.

The boattail geometries investigated are of the same general form as those shown in Figure 4.1. As discussed in an earlier section, the cusp shape in Figure 4.9 incorporates both an initial expansion turn away from the main freestream of the

forebody and a compression as the flow is then turned back to the parallel direction to the main freestream flow. Figure 4.9 shows the specific geometry used in the experimental wind tunnel tests [35] and in determining the base Mach number and pressure for the cusp boattail shape. With the cusp boattail, which is analogous to the aerospike ramp geometry, the freestream flow from the constant diameter body is initially turned away from the main flow and in towards the jet. This initial turn creates a Prandtl-Meyer expansion fan at the beginning of the boattail, which expands the flow to a higher Mach number and lower pressure. However, as soon as the flow is expanded through the initial turn, the geometry of the cusp begins to turn the flow back to a parallel direction with the main freestream flow. By turning the flow back onto itself, this creates compression waves, which raise the pressure and lower the Mach number until the base of the ramp. In the case of an aerospike ramp, the initial flow expands from the exit of the thruster along the ramp. An expansion fan emanating from the cowl lip, at the exit of the thruster, strikes the ramp, which reduces the formation of dissipative shocks along the aerospike contour, thus creating the expansion along the ramp.

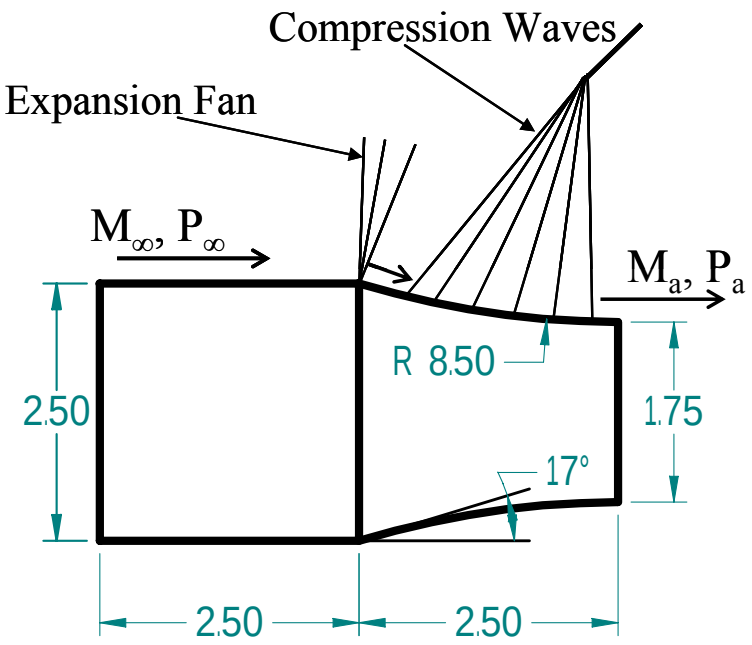

Figure 4.9: Cusp Boattail Geometry [35].

For the cusp shaped boattail, the Prandtl-Meyer expansion relations were used to determine the initial turning parameters and Mach number after the initial expanding turn. Then the oblique shock relations were used to determine the corresponding Mach numbers along the compression portion of the geometry to the end of the ramp. It was determined from the given geometric parameters that the initial turning angle was 17 degrees and it was assumed for the compression portion of the ramp that the geometry turned the flow in one degree increments until it returned it to a parallel direction with the main freestream flow, i.e., zero degrees with the freestream flow direction. This resulted in a Mach number after the boattail of $M_a = 2.54$, and a boattail pressure ratio of $P_\infty/P_a = 1.07$. The base Mach number is only slightly higher than the original freestream Mach number of 2.5, but it results in a higher jet-to-boattail pressure ratio, P_j/P_a, and thus a much lower base pressure ratio, P_B/P_∞. These results are in agreement with the general

physics of the flow. For higher Mach numbers at the end of the boattail, a stronger expansion is created, which is caused by the faster moving flow over the backward facing step of the base. Therefore, a lower base pressure will result from a stronger expansion at the base. The small differences in freestream flow parameters and negating the boattail term, i.e., Equation 4.14, lead to large differences in the predicted base pressure. Table 4.3 shows the base pressures calculated using Equation 4.15 for two cases compared to the experimental values from Rubin et al. [35]. The first case is calculated with the freestream Mach number and pressure prior to the boattail and references Equation 4.14 with the given geometric area ratio of the boattail. The second case is calculated with the calculated base Mach number, M_a, and boattail pressure ratio, P_∞/P_a, after the boattail geometry and sets Equation 4.14 to unity.

Table 4.3: Comparison between experimental [35], freestream parameters before the boattail (Case 1), and determined parameters after the boattail (Case 2), for the Cusp Shaped Afterbody.

Cusp Geometry, $M_\infty = 2.5$, $M_j = 2.7$					
P_{oj}/P_∞	**Experiment [35] P_B/P_∞**	**Case 1 P_B/P_∞**	**Case 2 P_B/P_∞**	**Case 1 Error %**	**Case 2 Error %**
47.2	0.256	0.243	0.148	4.7	41.9
89.0	0.350	0.323	0.198	7.6	43.5
130.2	0.419	0.384	0.235	8.4	43.9
172.4	0.474	0.437	0.268	7.6	43.4

The ogive shape in Figure 4.10 causes a continuous expansion towards the base because with each incremental step toward the end of the boattail, the geometry turns

away from the main freestream flow by some degree, i.e., it is an inside out cusp. The ogive produces similar flow physics to an aerospike flow in that the pressure decreases along the surface of the afterbody. This is because the ogive shape continuously expands the freestream to the base of the afterbody in the same way that the flow from the thrusters is continuously expanding along the contour of the aerospike nozzle. Figure 4.10 shows one of the specific ogive geometries used in the experimental wind tunnel tests [35] and in determining the base Mach number and pressure. Only one of the ogive shapes and results is shown for the procedural description.

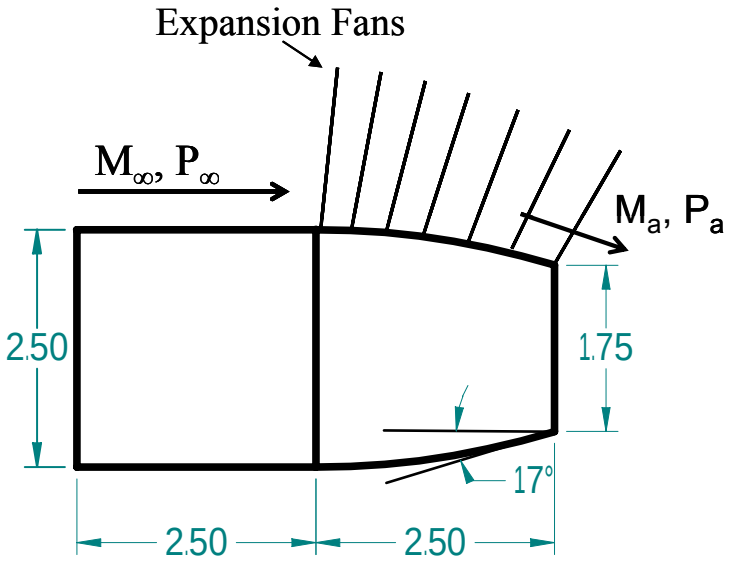

Figure 4.10: Ogive Boattail Geometry [35].

The same procedure of using the Prandtl-Meyer expansion relations was used with the ogive geometries to determine the base Mach numbers. The ogive shape had the same arc radius measurement as the cusp, only reversed. Therefore, in a similar manner as the cusp, only reversed, it was assumed that the geometry of the ogive expanded the

flow in one degree increments away from the main freestream, until it reached a maximum total turned angle of 17 degrees in toward the inner jet. Table 4.4 shows the results from the ogive afterbody study in the same manner as Table 4.3. Again, the Case 2 calculation method has a much larger error than the Case 1 calculation method. However, the error is almost half that of the cusp shape. This may be due to viscous shock interactions along the compression section of the cusp shaped boattail that the oblique shock wave theory does not take into account when calculating the base Mach number. This results in slightly larger experimental values of base pressure for the cusp geometry.

Table 4.4: Comparison between experimental [35], freestream parameters before the boattail (Case 1), and determined parameters after the boattail (Case 2), for the Ogive Shaped Afterbody.

Ogive Geometry, $M_\infty = 2.5$, $M_j = 2.7$					
P_{oj}/P_∞	**Experiment [35] P_B/P_∞**	**Case 1 P_B/P_∞**	**Case 2 P_B/P_∞**	**Case 1 Error %**	**Case 2 Error %**
47.2	0.279	0.261	0.208	6.3	25.3
88.6	0.335	0.323	0.268	3.7	20.1
130.1	0.398	0.383	0.320	3.7	19.5
172.6	0.449	0.438	0.363	2.5	19.2

The conical shape shown in Figure 4.8 only incorporates a single expansion turn, which uses the Prandtl Meyer equations to determine the base Mach number and pressure. Several different conical geometries were investigated with similar results to

the cusp and ogive shapes, ranging from 25-40 percent error for the Case 2 methodology. These are not shown for the sake of brevity.

The results of the cusp, ogive, and conical shapes for Case 2, show that without the boattail term of Equation 4.14, the method of using the base reference parameters consistently produced 20-40 percent error compared to using the freestream parameters prior to the boattail along with referencing the boattail area ratio in Equation 4.14. These results make reasonable sense because the boattail term of Equation 4.14 takes into account the flow turning effects of the boattail angle and the change in base annulus area from the reference diameter to the base diameter. Without this term, the pressure and Mach number calculated would apply to a parallel flow at the base with the constant diameter aft-body.

Therefore, accounting for the boattail effects and using proper values for the freestream parameters is important for using Brazzel's method for this analysis. It can also be concluded that because of the similarities in aerospike ramp geometry with the wide variety of boattail geometries used to develop the empirical correlation (Equation 4.11), the exit parameters of the aerospike thrusters should be assumed to be the freestream parameters for determining preliminary base-lip pressures during aerospike operations for net thrust calculations. This consequentially means that instead of using the aerospike base as the reference diameter in Equation 4.15, the diameter of the thruster cowl lip should be used as the reference diameter. Figure 4.11 shows the nomenclature associated with using Equation 4.15 for determining the base-lip pressure of the RPNCC nozzle configuration.

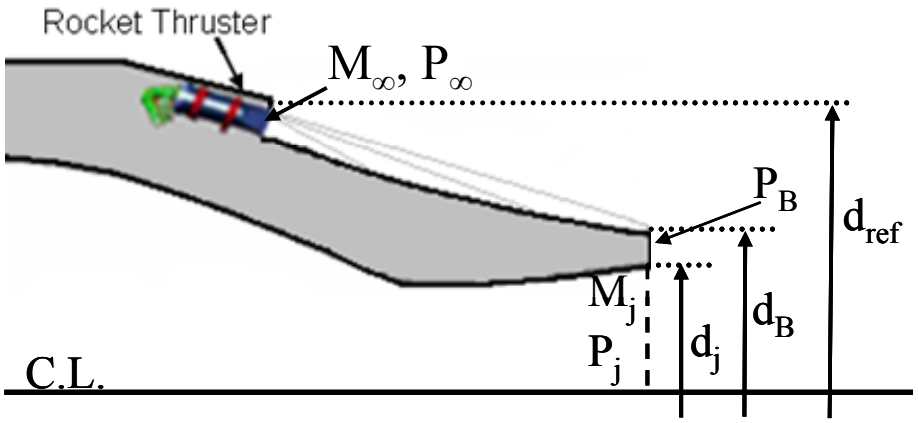

Figure 4.11: Geometric Parameters for Determining Base-Lip Pressure using Equation 4.15 for RPNCC Configuration.

4.5 Zero RMF to Base-Bleed Conditions

A detailed physical description of the flow behind an annular base with an internal jet is given by Rubin et al. [35], Cubbage [36], Reid et al. [37], and Fick [31]. The base-bleed condition occurs from just past zero mass flow through the internal nozzle to the point at which the flow becomes sonic at the airbreather throat. During this base-bleed state, the flow through the internal nozzle is entrained rather than emitted as a jet on the recirculating base region, analogous to introducing low-energy air into the "dead" or recirculating region behind a sealed base to help increase the base pressure [37].

Base-bleed would be available for the aerospike nozzle in the RPNCC configuration as long as the flight vehicle was in forward flight. Air would move through the inner airbreathing engine by ram-pressure in the inlet. Base-bleed can lead to substantial reductions in base drag for the aerospike nozzle and can help contribute to superior performance over the conventional bell nozzle. Also, it has been noted that by

making the area of the bleed duct as large as possible increases the base bleed effectiveness [37].

As discussed in Chapter 2, when the ambient pressure is higher than the design pressure of the aerospike contour, the wake boundary is open to the ambient atmosphere and the base pressure is very near the ambient freestream pressure. However, when the ambient freestream pressure becomes equal to or less than the design pressure of the aerospike contour, the wake closes and the base pressure becomes independent of the ambient pressure [31]. During the "closed-wake" condition, when the mass flow through the internal nozzle is zero, the external aerospike flow accelerates the air behind the base region through turbulent mixing along the wake boundary [36]. To preserve continuity an adverse pressure gradient caused by a trailing shock is formed to return the entrained air to the base region and an enclosed eddy flow results as shown in Figure 4.12.

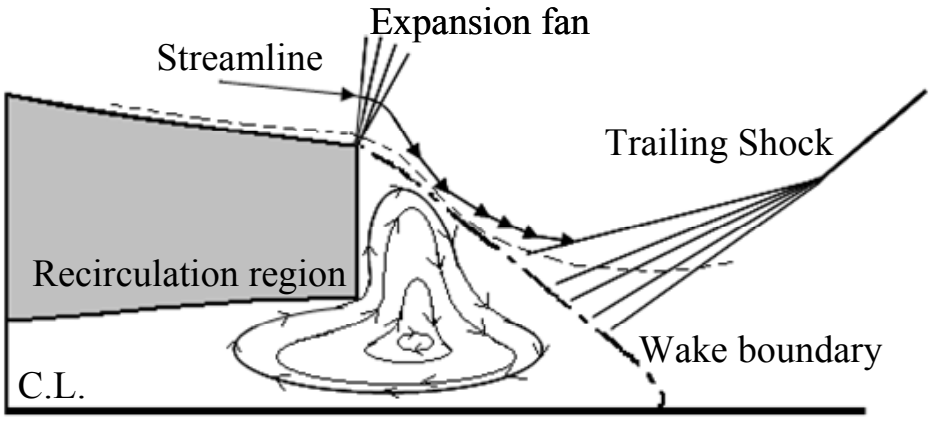

Figure 4.12: Flow Field with No-Base-Bleed (zero *RMF*) through Inner Jet Nozzle.

As mass flow through the internal nozzle is introduced to the base of the aerospike at low axial velocities, the base pressure begins to rise due to the mass and

momentum of the entrapped recirculating air decreasing. This in turn decreases the strength of the trailing shock, which decreases the adverse pressure gradient that returns the flow to the base region [37]. This trend will continue until the flow becomes sonic in the throat. Figure 4.13 shows the general flow conditions for a low momentum flow through the internal nozzle just as it becomes sonic at the throat.

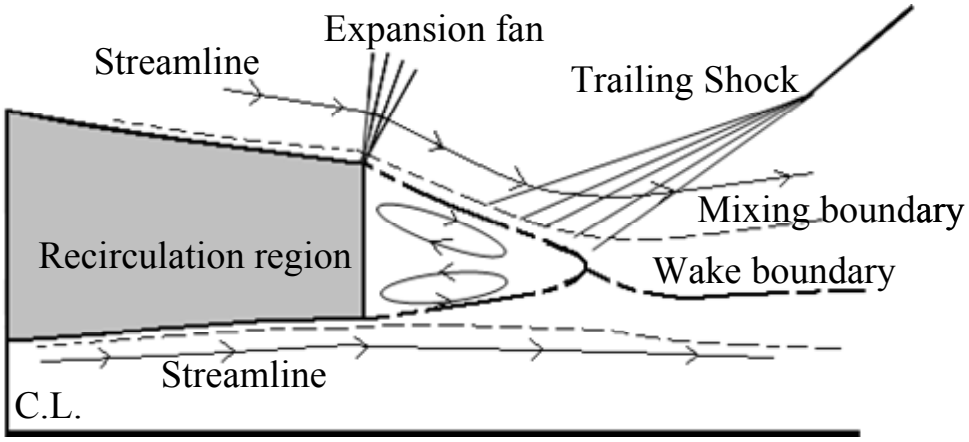

Figure 4.13: Flow Field with Base-Bleed Flow through Inner Jet Nozzle.

As discussed in Chapter 3, ADAPT has built in functions for determining the base pressure for truncated aerospikes [12]. Two of the built in correlations by Fick [40] have been found to agree more with generic aerospike shapes than the other functions available in ADAPT [12]. The first function for the "closed-wake," no-base-bleed condition, is an empirical base pressure model for cylinders and cones that was modified by Fick [40] with an added exponent to account for the negative angle of the flow turning from the edge of the aerospike to the base region. The base pressure with no-base-bleed or jet off is determined by

$$P_B = P_{ref}\left(0.025 + \frac{0.906}{1+\frac{\gamma-1}{2}M_{ref}^2}\right)^{0.35} . \tag{4.23}$$

The reference pressure and Mach number are prescribed by Fick to be the Mach number and sonic pressure ratio at the end of the aerospike ramp. For the boattail geometry from the experimental wind tunnel tests, this would correspond to the Mach number, M_a, and base-to-boattail pressure ratio, P_B/P_a, determined after the boattail. Equation 4.23 includes the effects of a boattail term, so that the base-to-boattail pressure ratio is equivalent to the base pressure ratio, P_B/P_∞, given by Equation 4.15 for the no-base-bleed condition. The second model given by Fick [40] was derived for a cylinder immersed in a supersonic flow with an added factor of the reference Mach number (M_{ref}) and sonic pressure ratio (P_{ref}), and is given by

$$P_B = P_{ref}M_{ref}\left(\frac{2}{\gamma+1}\right)^{\gamma/\gamma-1}\left[0.05 + \frac{0.967}{1+0.5(\gamma-1)M_{ref}^2}\right]. \tag{4.24}$$

A study was performed to see which of Fick's base pressure models compared best to the experimental data that Brazzel et al. [32] used to correlate Equation 4.11. It should be noted that most of the nozzles were never operated at absolute zero *RMF* ratio but there were specific experiments by Baughman et al. [33] and Cortright et al. [34] that ran jet-off conditions that equate to zero *RMF* for the inner nozzle. The values of base Mach number determined in the last section using the Prandtl-Meyer relations were used in Equations 4.23 and 4.24 to calculate a base pressure ratio that could be compared to the experimental values of jet-off conditions. During this study it was found that

Equation 4.24 was approximately four percent less than the experimental values of base pressure, while Equation 4.23 was on the order of 20 percent higher than experimental values. This is reasonable because Equation 4.24 was derived for cylindrical shapes in a supersonic flow, whereas Equation 4.23 was derived for cylindrical cones in a supersonic flow. Therefore, Equations 4.23 and 4.24 seem to remain consistent with the physical flows and geometric shapes used to develop them.

Table 4.5 shows some of the comparisons for jet-off conditions with experimental values of base pressures [33, 34] for boattail geometries. Equation 4.24 is consistently on the order of 20 percent lower than the experimental values for base pressures with no-base-bleed for boattail afterbodies, while Equation 4.23 is typically within a few percent of the experimental value. Again this makes sense because Equation 4.23 was correlated using data from similar geometric shapes immersed in a supersonic flow. From Table 4.5 it is apparent that Equation 4.23 should be used in determining the base pressure during jet-off conditions or zero mass flow through the airbreather in the RPNCC configuration.

Table 4.5: Comparison between jet-off base pressure models and experiment data [33, 34].

$M_\infty = 1.91$, $d_B/d_{ref} = 0.525$ for Baughman et al. [33], $d_B/d_{ref} = 0.704$ for Cortright et al. [34]

Experiment Reference	**Experiment P_B/P_∞**	**Eqn. 4.23 P_B/P_∞**	**Eqn. 4.24 P_B/P_∞**	**Eqn. 4.23 Error %**	**Eqn. 4.24 Error %**
[33]	0.787	0.786	0.626	0.1	20.5
[33]	0.808	0.780	0.628	3.5	22.3
[34]	0.775	0.780	0.628	0.6	19.0
[34]	0.770	0.770	0.631	0.0	18.1

Figure 4.14 shows a comparison of experimentally measured base pressures for a boattail afterbody with Equations 4.11, 4.15, and 4.23 as functions of *RMF* ratio. Again, Equation 4.23 is only applicable for zero *RMF* ratio or jet-off conditions, thus it only shows up as a single point on the graph at the lowest *RMF* value. This *RMF* value would equate to ram air bleeding through the airbreather during initial acceleration from the boost phase of flight. Also for these lower *RMF* values, the base pressure values from Equations 4.11 and 4.15 fall well below the values given by experiments and by Equation 4.23 for the no-base-bleed condition. This is to be expected, because the majority of data that Brazzel et al. [32] used to correlate Equation 4.11 were from the point where the NPR had been increased high enough that the inner jet was slightly under-expanded and the exit pressure was slightly higher than the base pressure. This point is typically around the minimum experimental base pressure value in Figure 4.14.

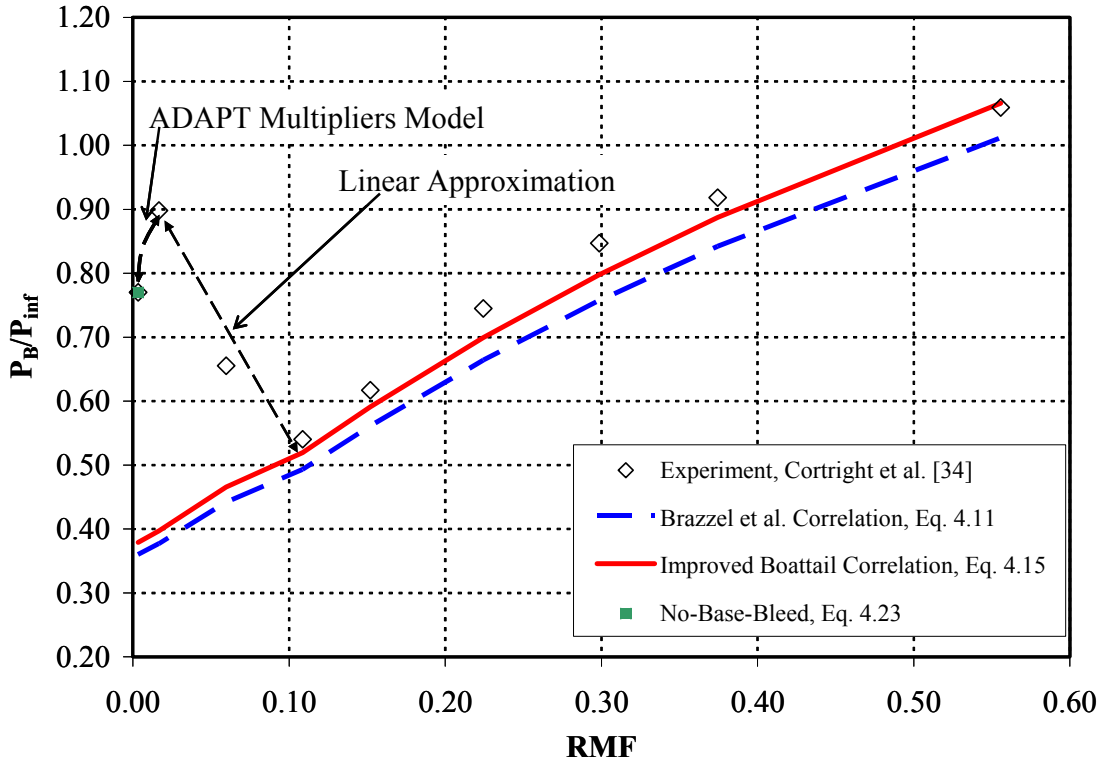

Figure 4.14: Comparison of Base Pressure Correlations from No-Base-Bleed Conditions to Full Jet-On Conditions.

For the non-zero *RMF* base-bleed condition, ADAPT also has a simple model [41] that determines the truncated aerospike base pressure by curve fitting experimental data as a function of base-bleed percentage relative to the primary aerospike flow [12]. This model provides multipliers of Equations 4.23, to give base pressures up to the point at which the flow becomes sonic at the throat of the nozzle. This point usually corresponds to the maximum experimental base pressure value in Figure 4.14. This model can be used in between the zero-*RMF* and the sonic throat conditions to give fairly accurate base pressure predictions for base-bleed [12]. The base-bleed conditions are analogous to the airbreather being primed to ignite the internal combustor.

Thus, for zero-*RMF* ratio, when there is no flow through the airbreather, Equation 4.23 can be used to estimate the base pressure for the no-base-bleed condition. As soon as mass flow begins to move through the airbreather and pressurize the base, the *RMF* ratio becomes non-zero and the base-bleed model in ADAPT is used to determine the base pressure until the flow becomes sonic at the throat. At higher flow rates Equation 4.15 can be used to estimate the base pressure. The region between the maximum base pressure, i.e., sonic throat, and the minimum base pressure, i.e., jet exit pressure equals base pressure, in Figure 4.14, can be approximated as a linear decrease in base pressure. This should adequately cover the lower *RMF* ratios for an "engineering-level" analysis of the RPNCC nozzle configuration.

4.6 Summary of Base Pressure Correlation and Future Validation

The large array of data taken over the 1950's and 60's for different model configurations and jet-to-freestream conditions for base pressures led to Brazzel et al. [32] being able to correlate an empirical relationship for base pressure founded on several of the most significant contributing factors. By modifying the original Brazzel method for cylindrical and boattail geometries only, it is assumed that it models an aerospike ramp more closely and the base-lip pressure can be determined for the RPNCC configuration. This method assumes the airbreather is the internal jet and the aerospike thruster parameters are the freestream parameters. During airbreather operation only, where the aerospike is turned off, the ramp contour is analogous to a boattail and the thruster parameters are replaced by the freestream parameters over the forebody of the flight vehicle. For the *RMF* range of 0.04 – 1.5, Equation 4.15 will give base pressure

values within approximately 10 percent of experimental values from boattail model data. The *RMF* value is mostly affected by either thrust level on the internal jet, freestream Mach number, or altitude pressure.

Equation 4.15 was integrated with the ADAPT source code and used to assess the propulsion characteristics of the RPNCC configuration. The ADAPT code needs to be run a total of three times to determine the propulsion characteristics of the RPNCC configuration. The first run is to obtain the initial isentropic plug data and the full length geometry of the plug for the design conditions. This also builds certain input files and fixed geometry files of the aerospike contour for the design conditions, so that off-design conditions can be processed in the later runs. The second run is to obtain the thruster properties at the exit plane of the individual thrusters only, which are then used as the freestream conditions in the base pressure correlation for the final run. The second run also builds a new file with the designator 'exit.moc', which contains the exit plane properties of the thruster nozzle. The user can then specify the radius of the base and the exit of the airbreathing nozzle in the input file and run ADAPT for a third and final time. The airbreather parameters are determined by performing a simple Brayton cycle [42] for ramjets or from known legacy data on past ramjet performance for the particular flight conditions being examined. These parameters are manually input into the ADAPT code for the third run. For the third run, the full length spike is truncated to yield the base radius the user specifies. The base radius depends on the exit diameter of the airbreather and the cross-sectional diameter of the flight vehicle. The base pressure is then calculated to determine a net thrust of the aerospike nozzle. This thrust is added to the thrust of the airbreather for a total net thrust during propulsion mode transitions.

A follow-on research project would be to run higher fidelity CFD simulations of some of the aerospike geometries produced by ADAPT to determine base-lip pressure values at different flight conditions. By adding turbulence effects, variable specific heat ratios for reacting gas, and axisymmetric aerospike geometries, the CFD simulations could be used for preliminary validation of using Equation 4.15 to determine base pressures for this nozzle configuration.

Ultimately, future testing of a wind tunnel, cold-flow aerospike rocket nozzle model with a hollow center to simulate the airbreather, would be needed for adequate validation of the geometry assumptions in the above base pressure methodology. Pressure readings in the aerospike thrusters and airbreather expansion chambers and along the surfaces of the model, and mass flow readings through both the airbreather and aerospike thrusters should provide enough data to validate the geometrical assumption for cold-flow testing. The model would need to be axisymmetric to allow for 3-D effects of the supersonic flows around the base and aerospike ramp. The experimental tests would serve not only as a fundamental fluid dynamic research project, but also as a foundation for a better empirical correlation for determining base pressure for this particular geometrical configuration. The experimental set-up could also be used to help further validate the ADAPT code performance calculations.

CHAPTER 5

PRELIMINARY RPNCC SYSTEM COMPARISON

5.1 Flight Vehicle Characterization

A comparison between an existing flight system and a similar system utilizing the RPNCC propulsion configuration was made to assess the potential of this unique concept. The U.S. Navy supersonic airbreathing cruise missile known as Talos was used as the base-line flight vehicle to make an "apples-to-apples" comparison between two identical flight systems using different propulsion configurations. The premise for this study was to determine if the same mission can be potentially achieved with a smaller vehicle or if there are added performance gains by using the RPNCC configuration in a similar geometric package. The airbreathing engine parameters and similar technology components such as aluminum fuel tanks and a pressure fed propellant system were maintained to distinguish the effects of the liquid fueled rocket stage versus the original solid fuel stage.

The Talos, shown in Figure 5.1, is a beam riding, rocket launched, ramjet propelled missile, designed for surface-to-air or surface-to-surface targets. It was developed during the 1940's under the U.S. Navy Bumblebee project, which was also responsible for the development of several other missile variants like the Terrier, the U.S.

Navy's standard missile system for today [8, 9]. Talos was designed to give the naval fleet stand off protection against enemy aircraft and distant surface targets [9, 43, 44]. It was the oldest airbreathing ramjet missile system in use until 1980. A modified version is now used to simulate supersonic anti-ship missiles for targeting and defense weapons development under the Vandal project [8, 9].

Figure 5.1: U.S. Navy Talos Missile in Booster Configuration [43].

The Talos ramjet engine was developed by Bendix Corporation to carry a 300 lbf payload to ranges in excess of 100 nautical miles. The ramjet was capable of 21,000 lbf of thrust and enabled the Talos to achieve ranges of up to 120 nm at cruise speeds of Mach 2.5. Its theoretical ceiling was 70,000 feet, although its typical trajectory peaked around 50,000 feet [43, 45]. For ranges in excess of 100 nm, the mission profile was

more than likely surface-to-surface and thus did not require higher altitudes for high velocity end-game due to its nuclear warhead payload [8, 9, 43, 44]. Instead, the Talos used more of its ramjet fuel to fly down range and maintain the high supersonic Mach speed, rather than gaining altitude. For surface-to-air mission profiles, the Talos was designed to fly out along a radar tracking beam from the launching platform to a predetermined intercept point, where it would then engage its target from above [8, 43, 44]. For such a mission, a higher altitude was desired but a 100 nm range was all that was required instead of a 120 nm range.

The analytical tools used in this conceptual design process were the modified ADAPT code for engine performance calculations, Missile DATCOM [46] for estimating aerodynamic coefficients of the flight vehicle, a liquid rocket tank sizing design code developed at UAH [47] for initial estimates of vehicle weights, and a two-degree-of-freedom (2-DOF) point mass trajectory code. The legacy performance data for the Talos came from several different resources, including journal articles and historical papers on U.S. Naval airbreathing missiles [7, 8, 9, 43, 44, 45, 50]. However, performance specifications for the ramjet engine were still considered classified, so estimations were made based on the known thrust, initial and final weight, and size of the vehicle. One-dimensional performance equations for mass flow rate and drag force

$$\dot{m} = \frac{T}{Isp\left(g_o\right)}, \tag{5.1}$$

$$F_D = \frac{1}{2} C_D A \rho V^2, \tag{5.2}$$

were used to estimate the *Isp*, required thrust to over come drag force, and mass flow rate of fuel. Equations 5.1 and 5.2 were used to develop the simple 2-DOF trajectory code in Excel, which gave a relatively good estimate of the Talos down range flight path, velocity, and fuel burned as a function of time.

The Talos had the capability to maneuver after the boost phase of flight via movable fins ahead of its fixed fins at the rear of the missile. This gave it the ability to alter its trajectory or intercept point with its target. However, the 2-DOF trajectory analysis used in the preliminary study only assumes downrange distance and altitude and does not analyze crossrange or the amount of fuel spent on maneuvering. This gives a higher prediction in downrange capabilities than is realistic for the original Talos. But, because both vehicles are being analyzed in the same manner, it can be assumed that the design with more fuel at the end of its trajectory will be capable of additional maneuvering over the other design.

The reason the Talos is such an attractive flight vehicle design for this study is because of its centerline axial airbreathing engine inlet. Other than providing improved stability for axisymmetrical flow into a canister ramjet, it has a simple combustor flowpath, which reduces the complexity and the amount of actuators and seals compared to a two-dimensional air-intake as seen on some airbreathing cruise missiles [48]. The reduced cooling loads and simpler combustor requirements result in a lighter flight vehicle and thermal management system weights. These factors help to increase the system's specific impulse (*Isp*) throughout the flight regimes allowing a higher Mach number to be achieved and shorter flight time to target. Also, to produce more of an "apples-to-apples" comparison between configuration types and to keep the airbreathing

engine as similar as possible between designs, only the tandem configuration of Figure 1.1 was compared against the RPNCC configuration for this study.

5.2 Base-Line Booster Phase of Flight

As discussed in Chapter 1, a ramjet requires a sufficient mass flow of air into the combustor to work. The ramjet powered Talos needed to be accelerated to operational speeds by a booster stage similar to that shown in Figure 1.1. The Talos solid fuel booster stage is capable of 116,000 lbf of thrust and accelerates the sustainer section of the missile to Mach 2.5 in about 6 seconds [43, 45, 49]. The Talos booster stage weighed a total 4400 lbf with 2700 lbf of propellant and an effective burn time of 5.7 seconds. The propellant grain was cut in a wagon wheel shape, which provided an almost constant mass flow rate for the duration of the burn. This allowed the solid booster to be designed for a maximum mean burn out velocity.

The change in velocity for the acceleration phase of a flight vehicle is given by

$$u_b - u_o = g(Isp)\ln\left(\frac{W_o}{W_b}\right) - \int_0^{t_b}\left(g\sin(\theta) + \frac{D}{W}\right)dt\,, \tag{5.3}$$

where u_b is the burn out velocity, u_o is the initial velocity, g is the acceleration due to gravity, W_o is the total initial weight, W_b is the burn out weight (initial weight minus the propellant weight), and θ is the local flight path angle with respect to the horizontal [7]. It can be seen from Equation 5.3 that a neutral to progressive burn for the boost phase is beneficial for achieving maximum velocity efficiently in an ascending trajectory. For example, with a lower constant flow rate in the initial acceleration phase from launch, the

Talos can climb through the denser atmosphere at a lower velocity with a lower drag coefficient. As the Talos ascends to the less dense atmosphere the mass flow rate increases, consequentially increasing thrust, to achieve a higher Mach number before transitioning or staging to the airbreather phase.

The mass fraction, W_o/W_b, is another key factor in tactical missile performance. Typical mass fractions of rockets are 50-70 percent of the initial weight as compared to 25-30 percent for airbreathers [7]. Thus, the logarithmic term in Equation 5.3 is larger for rockets, but because the *Isp* is only 20-30 percent that of an airbreather, the product of the two terms is significantly smaller for the rockets. This usually eliminates the rocket for long range missions. However, for boost phases, rapid acceleration is desired and the integrand term in Equation 5.3 is significant. This term can be minimized by making the time difference, *dt*, small and using a high average thrust-to-weight ratio [7]. The Talos missile including the tandem booster had an average thrust-to-weight ratio of 14 for the boost phase of flight.

The Talos had to begin ingesting air as soon as it was launched to prime the ramjet before booster separation. There were open slots between the missile and booster sections to allow air to flow through the ramjet. To help prevent inlet "unstart" in the ramjet, the missile had to fly at a relatively low angle of attack to maintain the shock system in the engine inlet. If this shock system moved too far out in front of the inlet, it resulted in a deficient flow of air into the engine, which severely impacted the performance and operability of the propulsion system. Flying at a lower angle of attack also helped to keep the back pressure behind the subsonic diffuser or the "isolator" section of the airbreather at sustainable levels for the fixed geometry inlet.

Talos aerodynamic parameters were determined by the Missile DATCOM code [46] with given geometric parameters [8, 9, 45, 43, 44, 50]. Figure 5.2 shows the geometry used in DATCOM to simulate the Talos flight vehicle in the booster configuration. Several geometric parameters were changed for the aerodynamic configuration of Figure 5.2 in relation to the actual configuration of Figure 5.1. An average constant cross-sectional diameter of 29 inches was chosen to simplify geometric inputs. The leading moveable fins had to be modified. This is because DATCOM cannot model a forward fin sweep. However, the modified fin design is aerodynamically similar to the original in that both have the same planform area. DATCOM cannot model a centrally placed axisymmetric inlet at the nose. Four smaller axisymmetric inlets were placed around the nose cone to simulate the single centrally located inlet of the Talos.

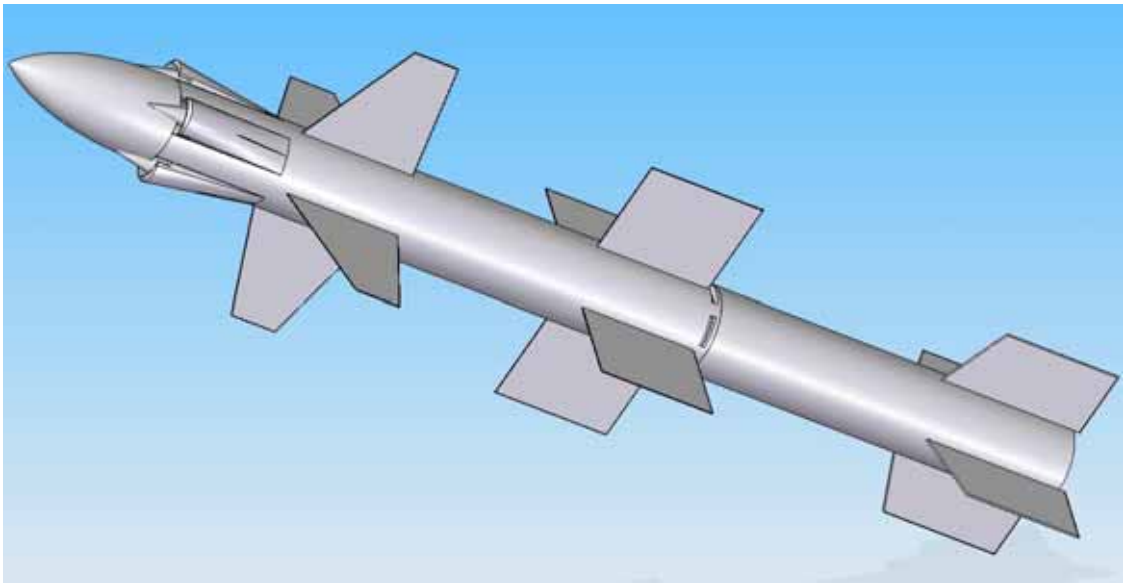

Figure 5.2: DATCOM Model of Talos Flight Vehicle.

Table 5.1 shows the flight Mach numbers and altitudes and associated drag coefficients predicted for the Talos during solid rocket boost phase. The drag coefficient does not change much with altitude, and was thus assumed to vary only with Mach number.

Table 5.1: Mach and Drag Coefficient Table for Booster Phase of Talos Flight.

Mach	C_D	Altitude (ft)
0.00	0.000	0
0.50	0.289	0
0.80	0.350	250
0.90	1.050	500
1.10	2.175	1000
1.40	1.600	2000
1.70	1.273	3000
2.00	1.090	4000
2.15	1.019	5000
2.48	0.895	6000
2.50	0.889	7000
2.57	0.869	7500

5.3 Base-Line Airbreathing Phase

The Talos airbreathing phase begins the moment the solid booster is no longer attached to the ramjet missile. The booster launches the Talos at an initial flight path angle of 30 degrees and separates at about 5,000 feet. Once the Talos separates from its booster, its angle of attack is almost immediately reduced to maintain the optimum shock capture for the ramjet inlet. Figure 5.3 shows the flight trajectory of the Talos airbreathing phase from booster separation. The trajectory shown is an ascending flight

path angle of 10 degrees to cruise altitude, then the same constant flight path angle from nose-over to impact.

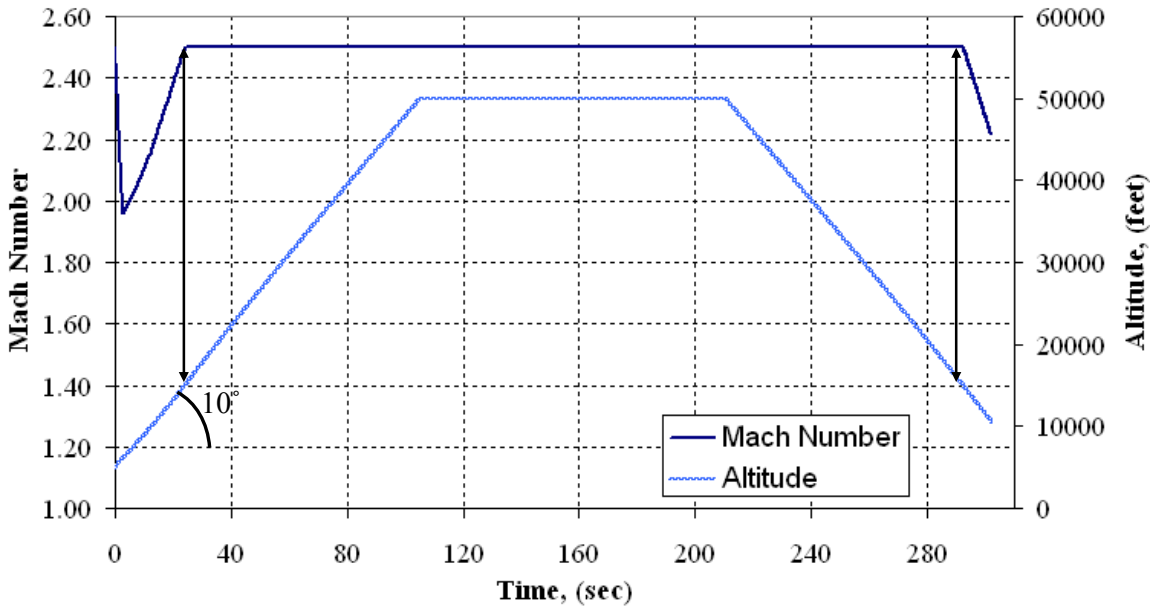

Figure 5.3: Mach number and Altitude as a Function of Time.

It was noticed that because the ramjet in the Talos was only able to produce about 21,000 lbf of thrust, the flight vehicle was not capable of sustaining Mach 2.5 in the lower atmosphere and began to slow down without the added thrust of the solid booster. This can be seen in Figure 5.3 by the dips in the upper curve below 15,000 feet. The arrows specify where in the trajectory the atmospheric density and drag coefficient is too high to sustain Mach 2.5 for the given performance of the Talos ramjet. Once the booster is separated, the missile begins to slow down due to insufficient thrust and the higher drag force in the lower atmosphere, but as the missile ascends to a higher altitude, the drag force decreases and the missile can begin to accelerate to maintain Mach 2.5. This trend is also seen in the descent phase of the trajectory. Once the missile is at about

15,000 feet, the drag force again becomes too great to sustain Mach 2.5, so the missile begins to slow down, losing kinetic energy before impact. Because the ramjet's thrust is proportional to the amount of air the engine ingests, it must maintain a certain recovery pressure ratio, i.e., the pressure ratio of inlet air to the combustor. This requires an increase in SFC, i.e., burning fuel rich, to maintain a high enough thrust level to accelerate back to Mach 2.5, where the missile can operate more efficiently and burn less fuel.

One of the final versions of the Talos had an 85 gallon (518 lbf) fuel tank, which also housed high pressure nitrogen bottles to keep the fuel tank pressurized during flight. The Talos burned JP-5 hydrocarbon fuel, which expands almost 7-8 percent for every 200 degrees Fahrenheit (˚F) increase in fuel temperature [51]. Therefore, the fuel tank was oversized to allow for the expansion of the fuel at Mach 2.5, where skin temperatures are about 575 ˚F at 50,000 feet and the internal combustion temperature is around 3000 ˚F depending on the air to fuel ratio. The liquid fuel was pressurized to prevent kinetic heating and formation of vapor bubbles when the liquid is in contact with hot parts [51].

5.4 Aerospike Rocket Booster Performance

It would be desirable to have an aerospike that just filled the Talos base diameter of 29 inches and have the ramjet exhaust through its base. However, this was not geometrically possible because the aerospike ramp would decrease the size of the ramjet nozzle exit and consequently decrease the airbreather thrust. To keep the ramjet performance properties the same for both vehicles, the nozzle exit area must be identical.

For aerospike ramp expansion the cowl lip must have a larger diameter than the 29 inch base-line flight vehicle. Also, an aerospike rocket nozzle 29 inches in diameter, operating with a chamber pressure of 1000 psi and using RP-1 and liquid oxygen for propellants, would only be capable of about 98,200 lbf of thrust. Therefore, the diameter, i.e., area ratio, of the aerospike would have to be increased to provide the required thrust for initial acceleration to Mach 2.5 for ramjet operation.

Table 5.2 shows different aerospike cowl diameters and ramp lengths with the corresponding ADAPT predicted values of thrust, *Isp*, base drag losses for no-base-bleed, and base radius. The third, sixth, and ninth aerospike configurations with 33 inch diameters gave the best performance while also providing an adequate base radius for the exit of the ramjet nozzle.

Table 5.2: Parametric study of Aerospike diameters and lengths.

Aerospike Number	**Cowl Radius [inches]**	**Ramp Length [inches]**	**Delivered Thrust [lbf]**	**Isp [sec]**	**Base Drag Thrust Lose [lbf]**	**Base Radius [inches]**
1	14.5	0.5	98,216	308	8148	10.3
2	15.5	0.5	112,291	308	9406	11.0
3	16.5	0.5	127,345	308	10794	11.8
4	14.5	1.0	97,523	319	7044	10.0
5	15.5	1.0	111,545	319	8214	10.8
6	16.5	1.0	126,508	319	9474	11.5
7	14.5	2.0	96,478	317	5369	9.5
8	15.5	2.0	110,356	317	6329	10.2
9	16.5	2.0	125,227	317	7430	10.9

With the aerospike rocket engines performance parameters, the oxidizer and fuel weights, tanks and residual weights, and propulsion hardware were estimated using a liquid-rocket tank prediction code [47]. The tank prediction code provided tank volumes that were used to calculate the length of a hollow cylindrical tank and torroidal end caps and ultimately the tank weight based on the tank wall thickness. The tank wall thicknesses were determined by assuming the outside tank wall to be in tension as a normal cylindrical thin walled pressure vessel would be and the inside tank wall, which surrounds the airbreather, to be in compression due to the higher pressure in the tank than inside the airbreather. Figure 5.4 shows the general shape of a torroidal propellant tank. Because the inside wall was assumed in compression, to prevent buckling, the inner wall thicknesses were doubled. This also adds more material for insulation around the tank and airbreathing engine. The thicknesses of the half torroidal end caps were calculated assuming a spherical geometry.

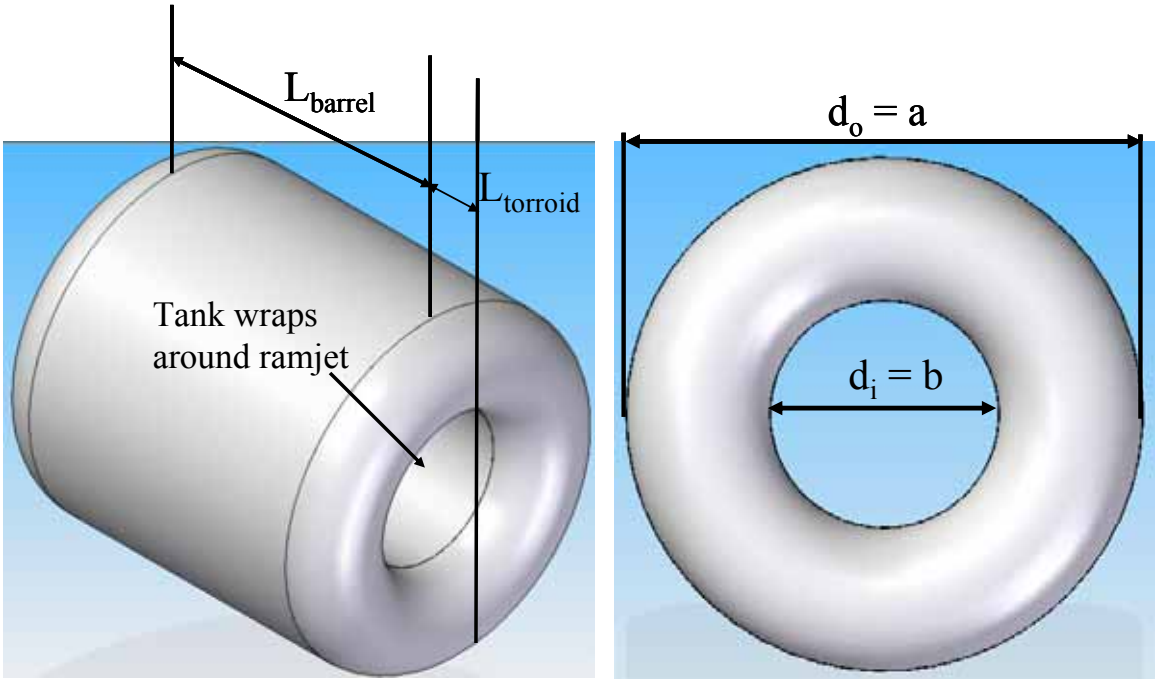

Figure 5.4: Propellant Tank Geometry.

The equation for the volume of a torroid is given by

$$Vol = \frac{\pi^2}{32}(a+b)(a-b)^2, \tag{5.4}$$

where *a* is the outer diameter of the torroid and *b* is the inner diameter. This equation was solved for a volume of the end caps using 33 inches and 16 inches as the outer and inner diameter, respectively, of the flight vehicle. This volume was subtracted from the total volume of the tank to determine the length of the cylindrical section of the elongated torroidal tank. The thickness of the outer tank walls were determined with

$$t_{wall} = \frac{\left[\frac{P_t(d_o)FS}{\sigma_{ys}}\right]}{\left(1+\left[\frac{P_t(FS)}{\sigma_{ys}}\right]\right)}, \tag{5.5}$$

where P_t is the tank pressure, d_o is the outer diameter, FS is the factor of safety, and σ_{ys} is the yield strength of the material. The weight of the tank is determined by calculating the volume of the tank material and multiplying by its density.

Table 5.3 shows the component weights for the propulsion system for the configuration 6 aerospike parameters in Table 5.2, and a six second burn of a conventional pressure fed rocket system with an Oxidizer to Fuel ratio of 2.3. The weights and tank volumes increase for longer burn times.

The engine mass estimate is based on an empirical correlation from legacy data of conventional bell rocket engines [3] and may not reflect current technological capabilities of mass savings in a new rocket engine design. However, it does match relatively well with legacy aerospike rocket engine data from Lamont [18] and thus provides a good first estimate of propulsion system masses.

Table 5.3: Component Weights of Aerospike Number Six for a 6 second Booster Burn.

He Pressurant	36.15	lbf
He Tank	100.24	lbf
Residuals	97.78	lbf
LOX	1658.31	lbf
RP-1	721.00	lbf
LOX Tank	1061.45	lbf
RP-1 Tank	754.70	lbf
LOX Tank Insulation	14.92	lbf
RP-1 Tank Insulation	9.35	lbf
Feed-Lines, Valves, and Support Structure	183.90	lbf
Engine	506.00	lbf
Total Weight of Booster	5143.79	lbf
LOX Volume	25.50	ft^3
RP-1 Volume	14.31	ft^3
Total Vol. of Propellants	39.81	ft^3

The weights in Table 5.3 are only for the liquid rocket booster and do not relate to any of the fuel requirements of the ramjet. Notice that the total estimated aerospike booster weight of 5144 lbf is about 740 lbf more than the original tandem solid booster configuration of the Talos using aluminum as the propellant tank material and a factor of safety of 1.5. A smaller factor of safety will result in a lighter weight of structural materials, but 1.5 is typical of unmanned aerospace systems.

Due to the increase in structural weight, the potential maximum net thrust of the aerospike engine is not enough to accelerate the RPNCC flight vehicle to Mach 2.5 in six seconds. To reach Mach 2.5 using the aerospike booster would require more fuel for

a longer burn time or lighter structural weight. Despite the improved performance of the aerospike, the liquid rocket engine and associated hardware are much heavier for the corresponding net thrust of the conventional solid rocket booster. Because the aerospike booster was unable to reach an altitude and speed before burn out, where the ramjet could operate as the only mode of propulsion for the flight vehicle, the added inert structural weight of the liquid rocket engine caused the airbreather phase to slow to a failing speed.

Since the aerospike rocket engine needed to have a larger diameter to accommodate the ramjet nozzle exit and to produce sufficient thrust to accelerate the flight vehicle to operational speeds for the airbreather, the reference diameter of the entire vehicle also increased. From Table 5.2, with aerospike configuration 6, the outer reference diameter of the flight vehicle is 33 inches and the inner diameter of the ramjet remains at 16 inches. The approximate lengths of the resultant fuel and oxidizer tanks are 4.0 feet and 6.5 feet, respectively. The length of the Talos missile including the solid booster is 33.3 feet. Subtracting 15 feet for the subsonic diffuser, electronics, servos, nozzle, and associated support structure leaves approximately 18 feet of available space for torroidal propellant tanks. After further subtracting the 10.5 feet for fuel and oxidizer tanks and 3.5 feet for associated structure, insulation, high pressure helium tanks, and excess plumbing, this leaves about 4 feet of space for additional fuel. The remaining 4 feet of length is available for the 500 lbf of jet fuel for the ramjet.

The original Talos ramjet would need about 250 lbf of fuel to go 120 nm down range, leaving roughly 250 lbf of fuel for extra maneuvers or cross-range in the original sized Talos fuel tank. However, due to the increase of the outer diameter of the RPNCC powered flight vehicle and the increase in inert mass from the propellant tanks, the

coefficient of drag increases and more power is required to accelerate through the atmosphere. To accelerate the new configuration to Mach 2.5 and a corresponding altitude where the ramjet could take over as the main propulsive mode, the amount of fuel required to travel 120 nm increases from 250 lbf to about 375 lbf due to the extra weight and increased cross-sectional area of the aerospike booster. This would only leave about 125 lbf for cross-range maneuvers.

From Figure 5.3, the Talos has slowed to about Mach 2.2 by 10,000 feet because of the denser atmosphere and insufficient thrust of the ramjet alone. On the other hand, by increasing the outer reference diameter to 33 inches, the larger flight vehicle would slow to about Mach 1.47 by about 12,000 feet because of the higher coefficient of drag. The aerospike booster would have to provide additional thrust for the flight vehicle to maintain Mach 2.5 to its target by throttling the thrust back to augment the airbreather and burning any remaining propellant in the rocket tanks. Maximum thrust from the aerospike rocket is not required to maintain Mach 2.5 to impact with a surface target from 15,000 feet.

After the initial boost to Mach 2.5 from launch, if the aerospike booster had fuel for an additional two seconds of burn at maximum thrust, it would have the capability to augment the airbreather for maintaining the higher Mach number in the lower atmosphere. For example, the base pressure thrust loss calculated by ADAPT, using the method discussed in Chapter 4, was about 650 lbf at the nozzle base-lip with the aerospike operating at about 3400 lbf. The base drag loss will increase with increasing aerospike thrust as long as the ramjet parameters remain constant. With the ramjet at max thrust and the augmenting aerospike, this contributed to a net thrust of about

24,400 lbf at the on-set of required augmentation at 15,000 ft, to 31,900 lbf toward the end-game phase of flight. Depending on the type of mission and payload, maintaining the high Mach number might not be required. In such a case the tandem solid booster would be simpler and contribute to the airbreathing stage having a higher performance. This is mostly due to the nature of the staging process of the tandem booster configuration. In principle, the discarded weight of the solid booster after burn-out allows for less propellant required to accelerate the remaining structure because inert structural mass is being shed [7]. An additional benefit of keeping the booster attached, such as the RPNCC configuration, would be using the individual thrusters on the aerospike for thrust vectoring and added maneuverability [30]. These abilities enhance the flight vehicle's capability to maintain higher Mach numbers for higher kinetic energy on impact with hardened targets in a surface-to-surface scenario or out maneuver a moving target in a surface-to-air scenario.

The first-order system study results indicate that the new RPNCC powered vehicle does not perform as well as the original Talos configuration. However the modified ADAPT was able to give the performance of several RPNCC configurations in far less time than CFD (Table 5.2). The thrust losses due to base pressure for augmenting thrust levels were used to provide for net thrust and performance values for the tank prediction code.

CHAPTER 6

CONCLUSIONS

The Rocket Plug Nozzle Combined Cycle (RPNCC) Propulsion System was conceived to help alleviate some if not all of the inherent disadvantages of conventional Rocket Based Combined Cycle (RBCC) configurations. The RPNCC configuration (Figure 1.7) consists of an external annular plug nozzle rocket engine surrounding an airbreathing engine (a ramjet, scramjet, or a turbo-ramjet) placed within the central plug body. The airbreathing engine exhausts through the plug base such that the interaction between it and the rocket engines occurs only at the exhaust. Unlike the conventional RBCC configuration (Figure 1.6), there are no additional internal flow field complexities in the operation of the two engines throughout the flight regime. The RPNCC system can potentially achieve more efficient packaging and reduced drag, while also providing rocket nozzle altitude compensation. The RPNCC configuration also could provide smooth engine operating mode transitions and improvements in overall engine performance.

A preliminary CFD study of the RPNCC system indicated that both nozzles would operate independently and gave the impetus for further investigation of this unique nozzle configuration. The CFD also showed that the outer aerospike flow would act as

the ambient atmosphere to the inner nozzle flow. Therefore, the exit pressure of the aerospike could be controlled to influence the under and over-expansion of the inner nozzle. This suggested a system level study comparing the RPNCC propulsion system performance to a conventional rocket or RBCC system in meeting a specific mission.

The time required to analyze a number of candidate RPNCC configurations using CFD was prohibitive. A rapid, relatively accurate method was needed for propulsion system analysis and optimization that could model the coaxial jets of the RPNCC system. The Aerospike Design and Performance Tool (ADAPT) was identified as a baseline analysis tool. ADAPT is an engineering-level code to design and predict the performance of 2-D or axisymmetric aerospike geometries. However, the baseline ADAPT did not model an inner coaxial jet in the plug base and the base pressure on the plug lip.

The primary research presented in this thesis is focused on the modification and integration of an empirical base pressure correlation into ADAPT to allow performance estimates for configurations such as the RPNCC system. The new base pressure correlation is derived from the Brazzel method used in a number of missile aerodynamic analysis codes. First, the aerospike geometry is similar to a missile boattail. A new term was derived to model the effects of boattail and cylindrical geometries only, i.e., no flare geometries, on base pressure. This improved the base pressure prediction to within 10 percent of existing experimental data. Next, a detailed analysis indicated using the cowl diameter of the aerospike as the reference diameter when using the exit parameters of the individual thrusters as the freestream conditions. This accounted for the flow expansion along the aerospike contour. For low RMF ratios or base-bleed conditions associated with the boost phase of a flight vehicle, ADAPT has built in functions that will

calculate the base drag losses. From the point at which the inner nozzle runs full or the exit pressure of the inner nozzle approximately equals the base-lip pressure, the base pressure can be determined using the modified base pressure correlation. The modified ADAPT code allows for the RPNCC configuration to be analyzed in a fraction of the time needed for CFD simulation.

The final part of this research was to use the modified ADAPT code with a suite of other engineering analysis tools in a first-order systems analysis comparison of the performance of a flight vehicle using the RPNCC configuration to the performance using conventional airbreathing and rocket propulsion systems. The U.S. Navy Talos missile was chosen for the baseline system. The Talos was a ramjet powered, supersonic cruise missile, that was launched in tandem with a solid booster that detached after burn-out and fell back to earth. The liquid aerospike rocket engine is a much higher performance engine than a solid propellant booster; however, it is also more complex and requires both oxidizer and fuel tanks along with corresponding support equipment, which lead to increases in weight. The RPNCC powered flight vehicle had to increase in diameter and consequentially weight to accommodate the required aerospike engine size and more fuel and oxidizer for continuous burning of the rocket engine. The higher energy density of the staged solid rocket booster provided an overall system advantage compared to the liquid RPNCC system in this missile application. The RPNCC system might provide some increased capability for rapid acceleration and maneuvering during the end-game and target impact, but these possible advantages do not override the significantly increased weight and performance reduction in the boost and cruise phases of the mission.

Although the RPNCC concept may not provide performance gains of solid rocket propulsion systems in typical missile applications, this novel concept may in fact be of benefit when replacing a conventional liquid rocket or RBCC system in a space launch vehicle application. A future study will assess this potential. The modified ADAPT code will prove a useful tool in this analysis.

REFERENCES

[1] O'Connor, E.F., "Saturn V Launch Vehicle Report," AIAA 66-840, AIAA Third Annual Meeting, Boston, MA, 29 Nov. 1966.

[2] Sutton, G.P., and Biblarz, O., *Rocket Propulsion Elements*, John Wiley & Sons, New York, 7th ed., 2001.

[3] Humble, R.W., Henry, G.N., and Larson, W.J., *Space Propulsion Analysis and Design*, McGraw-Hill, 1st ed., 1995.

[4] Heiser, W.H., and Pratt, D.T., *Hypersonic Airbreathing Propulsion*, AIAA Education Series, Washington D.C., 6th ed., 1994.

[5] Curran, E.T., "Introduction," *Developments in High-Speed-Vehicle Propulsion Systems*, Progress in Astronautics and Aeronautics, Vol. 165, AIAA, Washington D.C., pp. 1-13, 1996.

[6] Hank, J.M., Murphy, J.S., and Mutzman, R.C., "The X-51A Scramjet Engine Flight Demonstration Program," AIAA 2008-2540, 15th AIAA International Space Planes and Hypersonic Systems and Technologies Conference, Dayton, OH, 28 April – 1 May 2008.

[7] Billig, F.S., "Tactical Missile Design Concepts," *Tactical Missile Propulsion*, Progress in Astronautics and Aeronautics, Vol. 170, AIAA, Washington D.C., pp. 5-32, 1995.

[8] Fry, R.S., "A Century of Ramjet Propulsion Technology Evolution," Journal of Propulsion and Power, Vol. 20, No. 1, pp. 27-58, 2004.

[9] Waltrup, P.J., White, M.E., Zarlingo, F., and Gravlin, E.S., "History of Ramjet and Scramjet Propulsion Development for U.S. Navy Missiles," Johns Hopkins APL Technical Digest, Vol. 18, pp. 234, 2 Nov. 1997.

[10] Bulman, M. and Siebenhaar, A., "The Strutjet Engine: Exploding the Myths Surrounding High Speed Airbreathing Propulsion," AIAA Paper 95-2475, July 1995.

[11] Wood, D.E., Landrum, B.D., and Demaneuf, O., "Analysis of the Rocket Plug Nozzle Combined Cycle Propulsion System," AIAA 2008-5168, 44th AIAA/ASME Joint Propulsion Conference & Exhibit, Hartford, CT, 21-23 July 2008.

[12] Smith, S. D., "Final Report: Aerospike Design and Performance Tool", NAS8-00002, Engineering Sciences Incorporated, Huntsville, AL, August 2004.

[13] Rao, G.R., "Spike Nozzle Contour for Optimum Thrust," Planetary and Space Science, Vol. 4, pp. 92, Jan. 1961.

[14] Rao, G.R., "Exhaust Nozzle Contour for Optimum Thrust," Jet Propulsion, Vol. 28, pp. 377, June 1957.

[15] Anderson, J. D., *Modern Compressible Flow*, McGraw Hill, NY, 2nd ed., 1990.

[16] Zucrow, M.J., and Hoffman, J.D., *Gas Dynamics*, Vol. 1, John Wiley & Sons, Inc., 1st ed., 1976.

[17] Onofri, M., "Main Physical Features of Plug Nozzle Flows," AIAA 2002-4034, 38th AIAA/ASME Joint Propulsion Conference & Exhibit, Indianapolis, IN, 7-10 July 2002.

[18] Lamont, E.A., "The Aerospike Engine System for the Space Tug – A Status Report," AIAA 73-1245, 9th AIAA/SAE Propulsion Conference, Las Vegas, NV, 5-7 Nov. 1973.

[19] Frendi, A., Nesman, T.E., and Wang, T., "Computational and Experimental Study of Linear Aerospike Engine Noise," AIAA Journal, Vol. 39, No. 8, August 2001.

[20] Malik, T., "Going Hypersonic: Flying FALCON for Defense," Space News, 23 July 2003.

[21] Szedula, J.A., "FASTPASS: A Tool for Launch Vehicle Synthesis," AIAA-96-4051, 6th AIAA/NASA Symposium on Multidisciplinary Analysis and Optimization, Bellevue, WA, 4-6 Sept. 1996.

[22] Reid, J., and Hastings, R.C., "The Effect of a Central Jet on the Base Pressure of a Cylindrical Afterbody in a Supersonic Stream," Royal Aircraft Establishment, Report No. Aero 2621, Farnborough, England, Dec. 1959.

[23] Thompson, J.R., Jr., "Space Shuttle Main Engine Performance Assessment – Columbia's First Flight," AIAA 81-2471, AIAA/SETP/SAE 1st Flight Testing Conference, Las Vegas, NV, 11-13 Nov. 1981.

[24] Sulyma, P.R., and Baker, L.R., Jr., "User's Guide for TRAN72 Computer Code Modified for use with RAMP and VOFMOC Flowfield Codes," LMSC-HREC TM-D390409, Lockheed Missiles & Space Company, Huntsville, AL, Oct. 1974.

[25] Nickerson, G.R., "The RAO Method Optimum Nozzle Contour Program," SN91, Software and Engineering Associates, Inc., Carson City, NV, Nov. 1989.

[26] Anon, “Digital Computer Programs for Rocket Nozzle Design and Analysis – Bell Nozzle Design,” Vol. 2, NASA CR-65619, Pratt & Whitney Aircraft, Palm Beach, FL, June 1964.

[27] Smith, S.D., “User’s Manual – Variable O/F Ratio Method of Characteristics Program for Nozzles and Plume Analysis,” LMSC-HREC D162220-IV, Lockheed Missiles & Space Company, Huntsville, AL, June 1971.

[28] Evans, R.M., “Boundary Layer Integral Matrix Procedure BLIMPJ User’s Manual,” UN75-65, Aerotherm, Mountain View, CA, July 1975.

[29] Lee, C.C., and Thompson, D.D., “FORTRAN Program for Plug Nozzle Design,” NASA TM X-53019, MSFC, AL, July 1964.

[30] Higdon, K., “Analysis of Annular Plug Nozzle Performance and Thrust Vectoring Control,” Master’s Thesis, The University of Alabama in Huntsville, 2005.

[31] Fick, M., “Performance Evaluation of Plug Cluster Engines,” Master’s Thesis, Lehrstuhl Fur Raumfahrttechnik, Technical University of Munich, Munich, Germany, March 1994.

[32] Brazzel, C.E., and Henderson, J.H., “An Empirical Technique for Estimation Power-On Base Drag of Bodies of Revolution with a Single Jet Exhaust,” CP-10, AGARD, 1966.

[33] Baughman, L.E., and Kochendorfer, F.D., “Jet Effects on Base Pressures of Conical Afterbodies at Mach 1.91 and 3.12,” Lewis Flight Propulsion Laboratory, Cleveland, OH, NACA-RM-E57E06, 1957.

[34] Cortright, E.M. Jr., and Schroeder, A.H., "Investigation at Mach Number 1.91 of Side and Base Pressure Distributions Over Conical Boattails Without and With Jet Flow Issuing from Base," Lewis Flight Propulsion Laboratory Cleveland, OH, NACA-RM-E51F26, 1951.

[35] Rubin, D.V., Brazzel, C.E., and Henderson, J.H., "The Effects of Jet Plume and Boattail Geometry on Base and Afterbody Pressures of a Body of Revolution at Mach Numbers of 2.0 to 3.5," RD-TR-70-5, U.S. Army Missile Command, Redstone Arsenal, AL, April 1970.

[36] Cubbage, J.M., Jr., "Jet Effects on Base and Afterbody Pressures of a Cylindrical Afterbody at Transonic Speeds," NACA-RM-L56C21, Langley Field, VA, May 1956.

[37] Reid, J., and Hastings, R.C., "The Effect of a Central Jet on the Base Pressure of a Cylindrical Afterbody in a Supersonic Stream," Royal Aircraft Establishment, Report No. Aero 2621, Farnborough, England, Dec. 1959.

[38] Moore, Frank G., and Hymer, Thomas C., "Improved Power-on, Base Drag Methodology for the Aeroprediction Code," Naval Surface Warfare Center, NSWCDD/TR-00/67, May 2001.

[39] Korst, H.H., "Research on Transonic and Supersonic Flow of a Real Fluid at Abrupt Increases in Cross Section (With Special Consideration of Base Drag Problems)," Report ME-TR-392-5, University of Illinois Engineering, Urbana, IL, Dec. 1959.

[40] Fick, M., and Schmucker, R.H., "Performance Aspects of Plug Cluster Nozzles," Journal of Spacecraft and Rockets, Vol. 33, No. 4, July–August 1996.

[41] Martinez, A., "Final Report – Aerodynamic Nozzle Study," Vol. 1, C66-5878, Rockedyne, Canoga Park, CA, 15 July 1966.

[42] Wittenberg, H., "Some Fundamentals on the Performance of Ramjets with Subsonic and Supersonic Combustion," Delft University Press, 2000.

[43] Dean, F., "The Unified Talos," Johns Hopkins APL Technical Digest, Vol. 3, Num. 2, pp. 123-125, 1982.

[44] Garten, W. Jr., and Dean, F.A., "Evolution of the Talos Missile," Vol. 3, Num. 2, pp. 117-122, 1982.

[45] Shippen, W.B., Berl, W.G., Garten, W. Jr., and Hardgrave, E.J., Jr., "The TALOS Propulsion System," Johns Hopkins APL Technical Digest, Vol. 3, Num. 2, pp.126-134, 1982.

[46] Blake, W. B., "MISSILE DATCOM USER'S MANUAL - 1997 FORTRAN 90 REVISION," AFRL-VA-WP-TR-1998-3009, Air Force Research Laboratory, Wright-Patterson Air Force Base, OH, 45433-7531, 1997.

[47] Eddleman, D., "Reciprocating Propellant Feed System Development Program," Master's Thesis, The University of Alabama in Huntsville, 2006.

[48] Anderson, J.D., "Hypersonic and High-Temperature Gas Dynamics," AIAA Education Series, Washington D.C., 2nd ed., 2006.

[49] Barisa, B.B., "Type-Life Program for the Talos Booster MK 11 Mod 1, Results Through the 1 Year Test," U.S. Naval Propellant Plant, NPP-TMR-197, 15 Jan. 1962.

[50] Cronvitch, L.L., "Talos Aerodynamics," Vol. 3, Num. 2, pp. 138-141, 1982.

[51] Cazin, P., and Laurent, J.M., "Liquid-Fueled Ramjet Engine," *Tactical Missile Propulsion*, Progress in Astronautics and Aeronautics, Vol. 170, AIAA, Washington D.C., pp. 423-446, 1995.